Chapter 2
Models for the Description of Track Formation

Christian Dufour and Marcel Toulemonde

Abstract The different models developed to describe track formation induced by swift heavy ions will be presented. The macroscopic ones are the Coulomb explosion model, the bond weakening (BW) model, the exciton self-trapping (STX) model, the concept of reduced electronic energy loss, the analytical thermal spike model, the IDEA (Ionization Diffusion-Explosion-Amorphization) model, the inelastic thermal spike model (i-TS) and to finish microscopic descriptions using molecular dynamic (MD) calculations. All the models were applied to describe the track formation in different kinds of materials (metals, semiconductors or insulators), while additionally the i-TS model and MD calculations were used to describe the sputtering yield. It will be shown that the initial energy deposition plays an important role in the different descriptions and that there is no simple link between the energy deposited in the electronic and later in the atomic system. The large number of models presented here shows by itself that we are far away from a complete description of track formation. So the ambition here is just to give a present status of the different models.

2.1 Introduction

When irradiating a material with swift heavy ions, four stages have to be considered as depicted in Fig. 2.1. In the following it will be tried to describe how the energy deposited in the electrons in 10^{-16} s induces a nanometric transformation of the irradiated material called ion track. Such track is a discontinuous or continuous trail of defects [1] resulting from a dense electronic excitation, deposited in a short time and in nanometric space. Experimental results of track formation in various

C. Dufour · M. Toulemonde (✉)
Centre Interdisciplinaire de Recherche sur les Ions, les Matériaux et la Photonique (CIMAP), CEA-CNRS-ENSICAEN-Université de Caen, 14070 Caen, France
e-mail: toulemonde@ganil.fr

C. Dufour
e-mail: christian.dufour@ensicaen.fr

W. Wesch and E. Wendler (eds.), *Ion Beam Modification of Solids*,
Springer Series in Surface Sciences 61,
DOI 10.1007/978-3-319-33561-2_2

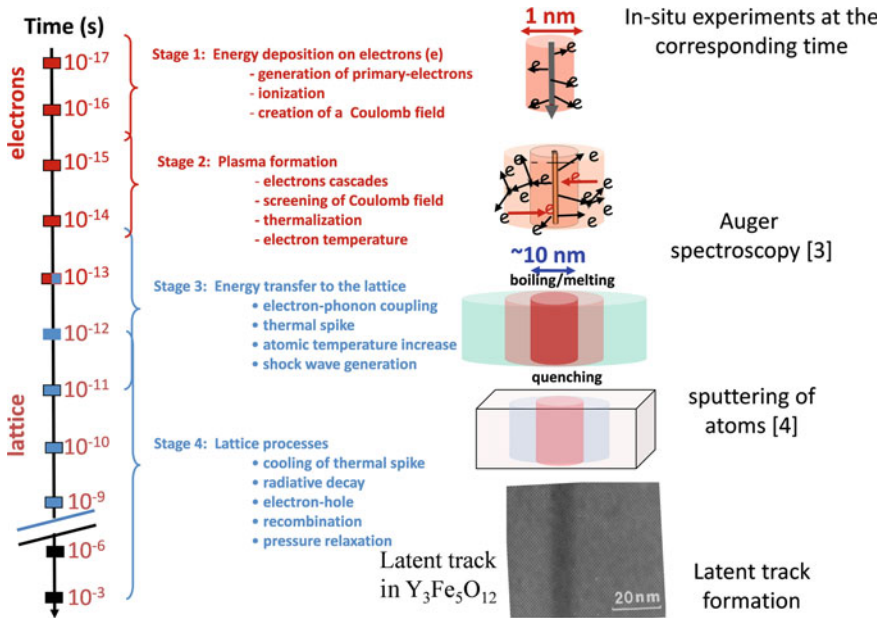

Fig. 2.1 Description of the different processes related to the energy deposition to the electrons and its relaxation to the lattice atoms. This figure is a combined picture from the paper of Zhang et al. [2] and of a track observed in $Y_3Fe_5O_{12}$ [161]. The column called "in situ experiments" account for Auger spectroscopy that probes the electron temperature at 10^{-14} s [162] and for atom sputtering [163] that probes indirectly the atomic temperature between 10^{-13} and 10^{-11} s. Tracks are observed in rest, i.e. after at least one day

materials will be reported in Part III of this book. As compared to nuclear collisions for which damage results from a direct atom–atom interaction, the track resulting from this electronic excitation is a four step process (Fig. 2.1) [2]: first, the incident ions transfer their energy to the electrons of the target by ion-electron collisions, second by electron-electron collisions this energy is shared among other cold electrons, third it is transferred to the lattice by electron-phonon coupling and fourth it dissipates among the atoms, inducing a spike along the ion trajectory. The energy is deposited in the electrons within 10^{-16} to 10^{-15} s and then transferred to the lattice atoms within 10^{-13} to 10^{-11} s. Our goal in this chapter is to present the different models that have been proposed to describe the latent track formation resulting from this four step process. A lot of questions are still open because it is not possible to make experiments within this short time scale within a nanometer volume and furthermore to develop microscopic models taking into account electron and atom motion at the same time. So it is necessary to proceed step by step in order to present the models that can provoke more clever experiments.

2.2 Electronic Energy Deposition

2.2.1 Electronic Energy Loss

Before any model development, it is necessary to know the slowing down of an ion per unit length (dE/dx). During a collision the incident ion with an energy E_i can transfer an energy E_e to electrons of the target with a probability $\sigma(E_i,E_e)$ [3–6]. The average energy $\langle E_{eav} \rangle$ deposited in the electronic system over a path length *dr,* small enough to allow a single collision, is

$$\langle E_{eav} \rangle = N\, dr \int_0^{E_{em}} E_e\, \sigma(E_i, E_e) dE_e \tag{2.1}$$

where N is the number of scattering centers per unit volume, E_{em} the maximum energy transfer to the electrons, calculated by the kinematics of an ion-electron collision. Therefore the energy loss of the incident ion (dE/dx) is equal to $\langle E_{eav} \rangle$/dr. Consequently the energy deposited to the target electrons is $S_e = -$dE/dx. The probability $\sigma(E_i, E_e)$ is deduced from Coulomb interaction between the incident ion and the electrons of the target atoms, described by Bohr [4] and Lindhard et al. [5, 6]. All descriptions take into account the effective charge states Z_1^* of the incident ions which are the result of a competition between electron stripping and electron capture determined by the ion velocity compared to the electron velocity of the target atoms. The evolution of the effective ion charge state as a function of its velocity is described either microscopically [7, 8] or macroscopically [9]. A continuous model of the energy loss process is based on the well known theories of Bohr and Lindhard, Scharff and Schiøtt [5, 6] and the electronic energy deposited in the target $S_e = -$dE/dx is calculated with the SRIM (Stopping and Ranges of Ions in Matter) code [10, 11]. The parameters necessary for calculations in the framework of this code have to be determined experimentally from fits of energy loss measurements. In a more recent development limited only to the electronic energy loss (the CasP code [8, 12]), the main input data are the projectile screening function, in the case of dressed ions, the electron density and the set of oscillator strengths for each sub-shell. The authors proposed a general interpolation procedure between close and distant collisions by introducing additive connecting functions. Thus, expressions derived for small and large impact parameters can be smoothly joined to a simple expression valid for all impact parameters.

The differences of the values of the electronic energy deposition per ion and unit length, S_e, calculated with the SRIM and CasP codes are illustrated in Fig. 2.2 for the example of Xe irradiation in CaF_2. The main features are on the one hand a difference by around ±10 % of S_e for beam energy larger than 1 MeV/u, and on the other hand a variation by a factor of 2 of S_e at energies around 0.01 MeV/u. Such variation in the electronic energy loss in this low energy regime depends strongly on the stopping material in which the atoms are slowing down [13]. It should be mentioned that in the lower energy range (around 0.005 MeV/u) the absolute value

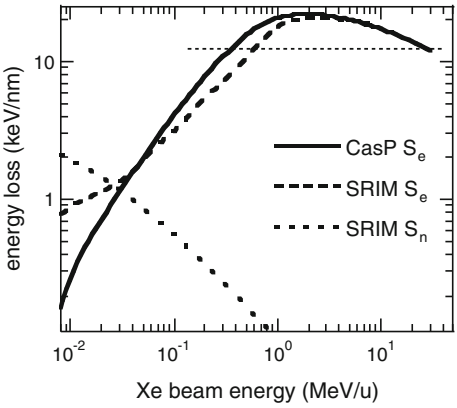

Fig. 2.2 Nuclear and electronic energy losses for Xe in CaF_2: comparison of the electronic energy loss calculated by SRIM [14] and by CasP [164]. The horizontal dotted line at ~ 12 keV nm^{-1} shows that same electronic energy loss can be reached with two different ion velocities

of electronic energy loss is smaller than the nuclear energy deposition per ion and unit length, S_n, as seen in Fig. 2.2 [14]. It should be noted that recent measurements of particle ranges in materials [15] at ~ 0.025 MeV/u are in favor of the CasP code [12]. Moreover such predictions have been confirmed by Sigmund [16, 17] since the electronic stopping cross section may be determined from the inverted ion-target system by applying the concept of reciprocity. The principle of reciprocity is based on the invariance of the inelastic excitation in ion-atom collisions against interchange of projectile and target, and is applicable in the low-velocity regime ($E < 0.025$ MeV/u) where the projectiles are neutral and the probability for electron loss is small. These differences can alter drastically any quantitative track description if the exact values of the electronic energy loss are not taken into account.

2.2.2 *Radial Energy Distribution*

For a given nominal S_e value, the energy density deposited in the electronic system strongly depends on the ion velocity, called velocity effect [18–26]. The target volume in which the kinetic energy of the ions is deposited to the kicked-off electrons of the target, the so-called δ-ray electrons, becomes larger with increasing ion velocity. Using Monte Carlo (MC) calculations, Katz and Kobetich [19, 20] and Fain et al. [21] have determined the radial distribution of the energy deposited in the electrons by calculating the evolution of the kinetic energy in the electron cascades as a function of the radial distance (~ 1 μm) and the time ($\sim 10^{-15}$ to 10^{-14} s) [22, 23]. These Monte-Carlo calculations have been updated by Kraft and Krämer [24] and Gervais and Bouffard [23]. The calculations stop when the energy given to an electron by a collision is smaller than the ionization potential which is in the order of 10 eV. Figure 2.3a presents the evolution of the dose in Gray versus the radial distance from the ion axis. Gray is usually defined as the energy deposited per

kilogram of matter (J/kg). The unit (J/kg) can be expressed in eV/at. These curves result from Monte Carlo calculations [25] for the same value of electronic energy loss ($\sim$11.3 keV nm^{-1}) at two different ion energies per nucleon in mica. Since the volume in which the energy is deposited is smaller at low energy than at high energy, the energy density deposited in the electrons is the larger the lower the ion energy is.

Fitting the results of Monte Carlo calculations [19, 20], an analytical formula has been proposed by Zhang et al. [22] and Waligorski et al. [26] that describes the energy distribution versus the radial distance from the ion axis,

$$D_0(r) = (B/r)\,(1 - (r + r_0)/(r_m + r_0))^{1/\alpha}/(r + r_0). \tag{2.2}$$

Here $D_0(r)$ is the dose deposited at a radial distance r from the ion path, r_0 is the range of electrons having the ionization energy of the target, r_m is the maximum range of the δ ray electrons in the considered matter and α is a constant depending on the velocity of the incident particle. The dose distribution $D_0(r)$ is corrected by a factor (1 + $K(r)$) to take into account the missing dose at small radial distances ($\sim$1 nm) [26], leading to an energy A(r) given to the electrons per unit volume

$$A(r) = D_0(r)\,(1 + K(r)) \tag{2.3}$$

with B a normalization constant ensuring that the integration of $A(r)$ over the radial distance is equal to S_e in cylinder geometry.

$A(r)$ can be calculated versus the radius for each material [22]. Figure 2.3b shows the fraction of S_e deposited in the electronic system versus the radial distance from the ion trajectory for vitreous SiO_2 irradiated with different ion energies per nucleon [27].

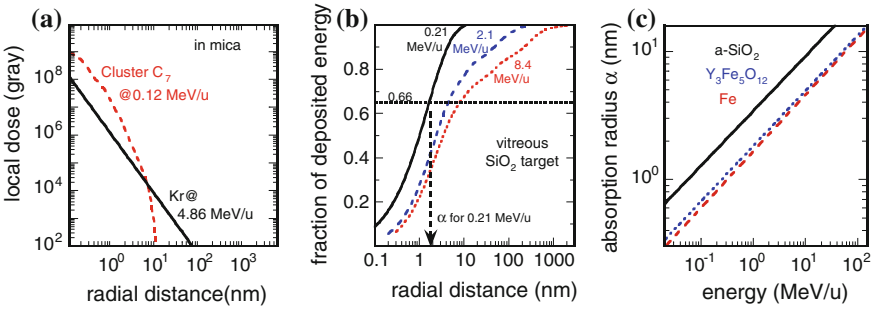

Fig. 2.3 **a** Radial distribution of the energy deposited in the electrons in mica for two different beam energies (from Bouffard et al. [25]). The lines are fits of the calculation results. **b** Fraction of energy deposited in the electrons of vitreous SiO_2 irradiated at different energies as a function of radial distance from ion trajectory [27]. The calculations assume cylindrical geometry and are based on Monte Carlo calculations [26]. **c** Evolution of a cylinder radius α in which 66 % of the initial energy is deposited in the electrons, versus beam energy for vitreous SiO_2 (a-SiO_2), $Y_3Fe_5O_{12}$ and Fe

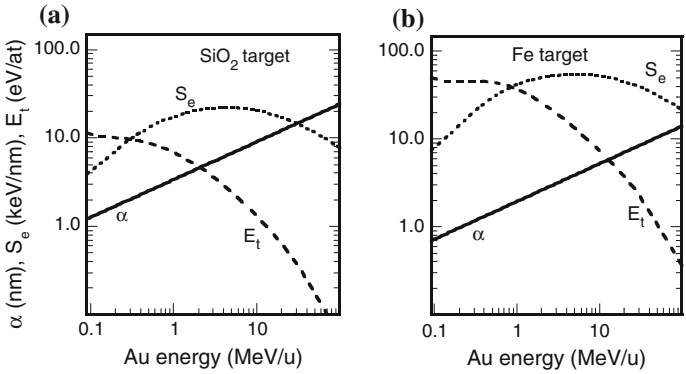

Fig. 2.4 S_e, α, and the energy deposited in the electrons (E_t) versus beam energy for Au irradiation of **a** vitreous SiO_2 and **b** Fe

To estimate the effect of the ion velocity, a cylinder of radius α in which 66 % of the electronic energy loss is stored, has been defined (Fig. 2.3b). This criterion assumes that ~2/3 of the energy deposited in the electrons is located in the core of the track and ~1/3 in the halo of the track as shown in [27]. As it can be seen in Fig. 2.3b, the deposition radius increases with increasing energy, i.e. larger ion velocities lead to electronic energy deposition in a larger volume resulting in a lower energy density. Figure 2.3c shows α values as a function of the specific beam energy for different materials. These α values follow roughly a power law of the specific energy ($\alpha \sim E^{0.4}$), i.e. seem to be almost proportional to the ion velocity. It should be noted that the extrapolation of the analytical formula of the radial energy distribution from Waligorski et al. [26] to low energies ($E < 0.1$ MeV/u) is questionable and in this energy regime new Monte Carlo calculations are needed.

As an example, S_e and the absorption radius α are plotted in Fig. 2.4 versus the Au energy for an irradiation of vitreous SiO_2 (Fig. 2.4a) and pure Fe (Fig. 2.4b). The energy E_t deposited in the electrons is equal to the electronic energy loss S_e divided by $\pi\alpha^2$, the area in which the slowing down energy of the ion is given to the electrons normalized with the atomic density of the material. E_t is shown in Fig. 2.4 in eV/at for SiO_2 and Fe. At 1 MeV/u the energy deposited in the electrons is $E_t \sim 7$ eV/at for SiO_2 and ~40 eV/at for Fe (Fig. 2.4) corresponding to 5.6×10^4 and 3.2×10^5 J cm^{-3}, respectively. Assuming a mean value of $\sim 2 \times 10^5$ J cm^{-3} this leads to a power of $\sim 2 \times 10^{19}$ W cm^{-3} within a time of 10^{-14} s. Such a power has to be compared to femtosecond laser irradiation: as an example, melting of Ni is expected when it is irradiated by a femtosecond laser (200 fs) with a power of 0.43 J/cm^2 [28]. The depth of the light absorption is in the order of 10^{-6} cm in a metal and so the energy density is 4.3×10^5 J/cm^3, i.e. a power of $\sim 2 \times 10^{18}$ W/cm^3 which is one order of magnitude lower than that for ion irradiation. So, as already mentioned [29, 30], it is reliable to take advantage of experiments and models developed to describe the transformation of matter by femtosecond lasers in order to understand track formation and sputtering due to ion

irradiation. However, the main difference in these two processes of electronic excitation is the geometry and the size: with ions this energy is deposited in a cylinder with some nanometer radius, while fs laser irradiation has a planar geometry with a beam spot of ~ 1 µm and a minimum depth of light absorption of ~ 10 nm. Such change in the geometry influences the cooling rate which is one order of magnitude larger in cylinder geometry as compared to a planar one.

2.3 Description of Track Formation

The track in a material is a trail of damage resulting from a nanometric, dense and shortly created electronic excitation and was observed for the first time by Silk and Barnes [31]. Defects created by individual electronic excitation as observed by classical irradiations (gamma irradiation or low Z ions) are not considered.

The electronic energy loss S_e with its radial distribution is the initial stage of any track description which will be presented now. Several macroscopic models have been proposed: Coulomb explosion [32–34], reduced electronic energy loss [25], self-trapped excitons [35–38], bond weakening [39, 40] and the thermal spike model developed by Szenes [41, 42] considering only the process starting when the energy is already transferred to the atoms. Then Canut and Ramos [43] introduced the concept of effective electronic energy loss by analytically solving the diffusion equation for the temperature distribution of the electrons and considering the energy transfer to the atoms. Toulemonde et al. [27, 44], Trautmann et al. [45], Meftah et al. [46, 47], Dufour et al. [48, 49] and Wang et al. [50] have numerically solved [51] the complete two coupled differential equations describing heat diffusion within the electronic and atomic subsystems of the solid. The thermal spike model is subject of intense research [27, 30] in order to study its strengths and weaknesses or to develop alternative models [52, 53]. It is not the aim of this chapter to describe all the models in detail, but we shall summarize recent detailed reviews [29, 37, 53] by giving an overview about the various models with the focus on the main physical phenomena the models are based on.

All these models cover several fields of physics: the ionization stage resulting from the ion-electron collisions leads to a positive charge along the ion path which is described by atomic physics [54]. This results in the creation of a high electric field which exists only for a short time due to its rapid screening by the returning electrons [32] and also in a distribution of the energy deposited in the electrons. These two processes induce then atomic motion which is described by a solid state physics approach [55–57]. The following response of the atomic lattice to the perturbation is a problem of mechanics [58–60]. And finally, the resulting structural modifications and possible atomic motion have to be explained in the framework of solid state physics. This clearly shows that the description of track formation is a complex problem [61–63].

At the end of this chapter molecular dynamics calculations will be shortly described in order to illustrate the development of microscopic models [2, 62, 64–67].

2.3.1 Coulomb Explosion

Ejection of electrons by ion-electron collisions leads to the appearance of ionized target atoms, creating a Coulomb field along the ion path. The ion motion under this electric field that exists during a limited time (less than 10^{-13} s) may induce tracks in materials. Such a model was developed by Fleischer et al. [32] to explain that hard insulators (like Al_2O_3) and metallic materials are insensitive to ion irradiation in the electronic energy loss regime. The volume in which such an electric field is created is as narrow as 1 nm^3 [63] and the created Coulomb field acts in a short time ($\sim 10^{-14}$ s) as recently measured by Schiwietz et al. [68, 69] and Rzadkiewicz et al. [70].

The model describes under which condition a repulsive Coulomb force is sufficient to prevail over the lattice bonding forces. This local force is equal to $n^2e^2/\varepsilon a_0^4$ where n is the average ionization, ε the dielectric constant of the considered material and a_0 the mean atomic spacing. If this force is larger than the mechanical strength $\sigma_M \sim Y/10$ (Y the Young modulus) then atomic motion is expected.

With the availability of large accelerator facilities, in the 1980s it was shown that pure metals [48, 71] and insulators like Al_2O_3 [72, 73] are really sensitive to electronic excitation which could not be explained by the model descibed by Fleischer et al. [32]. So the Coulomb explosion model was extended by Lesueur and Dunlop [33]. They estimate the space charge created by an incident ion during a time scale defined by the electron gas response. The ionized radius was calculated leading to a dimensionless quantity $\eta = Z_1^* \times v_0/v$ where Z_1^* is the effective charge of the incident ion, v its velocity and v_0 the Bohr velocity. This quantity η is proportional to $S_e^{0.5}$ since S_e is proportional to the square of the incident ion charge. The model was applied to pure metallic materials (Ti and Fe) for which the existence of a displacive transformation associated with a soft mode in the phonon spectrum seems to favour efficient energy transfers between highly excited electrons and target atoms [74]. The experimental damage cross sections are plotted versus η and fitted with a power law of η^8, i.e. to S_e^4 (solid lines in Fig. 2.5a for Ti [75] and Fe [76]). Such a law is expected since the calculated kinetic energy E_{kin} received by the atoms during the Coulomb explosion follows roughly a power law ($E_{kin} \sim S_e^4$) [33]. The model was also applied with success to high T_c superconductors by Iwase et al. [34]. In that case $(\Delta c/c_0)/\Delta N_I$ which is the relative increase of the c-axis lattice parameter per incident ion normalized by the initial value of the lattice parameter c_0 with the ion fluence defined as N_I is plotted versus dJ/dx where dJ/dx is the deposited energy per unit lenght with J the potential energy resulting from primarily ionized atoms [32] (Fig. 2.5b). dJ/dx is a parameter proportional to S_e. As can be seen $(\Delta c/c_0)/\Delta\Phi$ is proportional to $(dJ/dx)^4$ and thus to S_e^4 as proposed in the case of Coulomb explosion [33] developed for metallic materials.

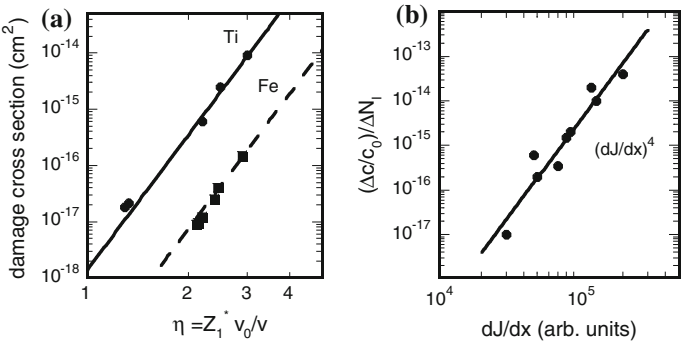

Fig. 2.5 **a** Cross section for damage creation in Ti and Fe by electronic excitation versus η from Lesueur and Dunlop [33]. The lines are proportional to η^8, i.e. proportional to S_e^4. **b** For high T_c superconductors, $(\Delta c/c_0)/\Delta N_I$ is plotted versus dJ/dx, and the solid line represents a $(dJ/dx)^4$ dependence (after Iwase et al. [34])

It should be noted that, as suggested by Fleischer's original Coulomb explosion model, that this electric field exists in a time range of 10^{-14} to 10^{-13} s in order to be efficient. Based on this time Itoh et al. [37] have calculated the energy transferred to the atoms and they suggest that rather a little fraction of the initial deposited energy is transferred to the atoms ($\sim$some 10^{-3} of S_e) along the ion path in agreement with the calculations of Lesueur and Dunlop [33].

2.3.2 *Bond Weakening (BW) Model*

Electron excitation can affect interatomic forces, leading to material modification as suggested earlier. The bond weakening is a natural extension of earlier ideas showing a strong dependence of the crystal structure on the corresponding electronic structure of the material [77]. Such a model was developed by van Vechten et al. [39] and Combescot et al. [78] to explain laser annealing of defects in Si by nanosecond laser pulses. But it has appeared that the electron–hole pair concentration created by the laser light absorption may be too small to be critical to ensure a thermal annealing. Then to explain such annealing a transient thermal process was suggested and quantitatively developed [79, 80]. This model was able to describe quantitatively the time and depth of melting. The comparison with experiments was performed by measuring the time of melting by in situ reflectivity and the depth of melting by impurity diffusion [81–83]. The measurement of light reflectivity provides also the evolution of the surface reflectivity versus temperature of the solid [82].

More recent calculations for Si, Ge and GaAs by Stampfli and Bennemann [40] find that the excitation (and hence loss) of valence electrons by 15 % induces lattice instability within 100 fs [84], consistent with recent time-resolved x-ray diffraction measurements following a femtosecond laser pulse [85] in Bi. It is certainly true

that excitation from bonding valence orbitals to antibonding conduction band orbitals leads to very rapid structural rearrangements in systems like Bi [86]. Extended discussions regarding this phenomenon are given by Duffy et al. [53] and by Klaumünzer [30].

2.3.3 Exciton Self-trapping (STX) Model

Excited electrons and holes polarize the surrounding lattice creating a distortion which, associated with the excited carrier, is called a polaron. Two kinds of polarons do exist [87], the one linked to a free motion of the carriers in the lattice and the second that can be trapped by the created distortion and is called self-trapped exciton. In halides [88] like in LiF [89–93] and oxides, particularly crystalline quartz [91], this phenomenon has been observed under swift heavy ion irradiation [88–93]. Atomic motion is the result of the transfer of the stored electronic energy to the lattice by emission of several phonons. This process was studied in several materials by Itoh and Stoneham [36]. They conclude that in insulators self-trapping of excitons influences the critical energy deposition for track formation. According to this study, the critical energy loss amounts to 3–5 keV nm^{-1} in materials where excitons are self-trapped, as e.g. in crystalline quartz. In materials in which self-trapping of excitons does not occur like in metallic materials and III-V and group IV semiconductors the critical energy deposition for track formation reaches values near 20 keV nm^{-1}. The difference can be ascribed to a strong localization of electronic excitation energy along the ion path in halides while it is delocalized in the case of free excitons.

A quantitative development of the model has been done for crystalline SiO_2 by Itoh [91] in order to describe amorphous ion tracks observed by Meftah et al. [46]. It is assumed that this exciton mechanism is efficient only if the number of self-trapped excitons is equal to the number of the SiO units. Suppose that $D(r)$ is the dose deposited per unit area in a coaxial cylindrical shell of a thickness of a molecular layer, at a distance r from the path of the ion as calculated by Zhang et al. [22]. The initial dose distribution $D_0(r)$ transferred to the electrons is mainly governed by the secondary ionization by δ ray electrons [see (2.2)]. The number $p(r)$ of self-trapped excitons per unit area produced at a distance $\boldsymbol{r}$ from the ion path is given by $p(r) = D_0(r)/W$, where W is the energy necessary to excite all SiO_2 electrons. For the calculation of the cylinder radius in which all SiO_2 electrons are excited a value larger than W = 38 eV was assumed. This value which is larger than the optical gap energy of crystalline SiO_2 ($\sim$9 eV [94]) was used since the energy to create an electron-pair is around three times the optical band gap. The results of the calculation are compared with experimental results by Meftah et al. [46] in Fig. 2.6, in which the experimental track radii (dots) as well as the calculated ones (full line) are plotted as a function of electronic energy loss S_e. The good agreement between experiment and calculation confirms the suitability of the model for the description of ionization induced damage formation in SiO_2.

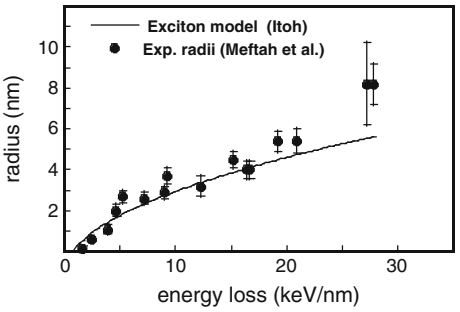

Fig. 2.6 Experimental radii in c-SiO_2 from Meftah et al. [46] compared to calculations in the framework of the exciton model from Itoh [90]

2.3.4 *Concept of Reduced Electronic Energy Loss*

The concept of reduced electronic energy loss was introduced by Bouffard et al. [25] in order to take into account the fact that for the same electronic energy loss the track radii are larger for low beam energy (<0.6 MeV/u) than the radii resulting for high beam energy (>2.7 MeV/u) as observed in mica (Fig. 2.7a).

The main difference is that at low ion energy the energy deposited in the electrons is spread out into a smaller volume than at high energy. As an example the maximum energy transfer per ion to electrons for a beam energy of 0.1 MeV/u is around 200 eV, while at 10 MeV/u it is 20 keV. Using the Monte Carlo model described by Gervais and Bouffard [23], the calculated radial dose $D_{MC}(r)$ does not give the corresponding energy loss with satisfactory accuracy. Thus the radial dose distribution has been normalized assuming that

$$D(r) = \frac{dE/dx}{\int_0^\infty 2\pi r D_{MC}(r')dr'} D_{MC}(r) \tag{2.4}$$

where $D(r)$ is the local dose at a distance r from the ion path (Fig. 2.3a).

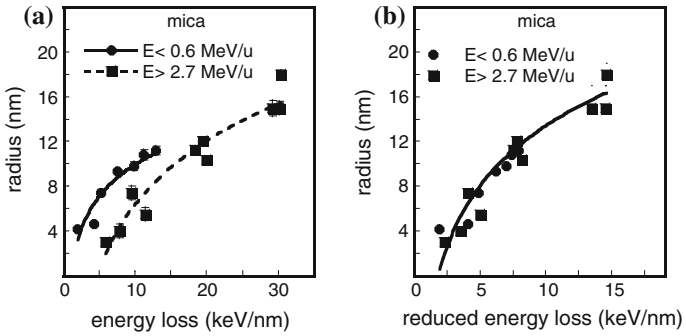

Fig. 2.7 Experimental track radii in mica versus (**a**) electronic energy loss, (**b**) reduced electronic energy loss. The data presented in the two pictures are from Bouffard et al. [25]. The lines are there to guide the eye

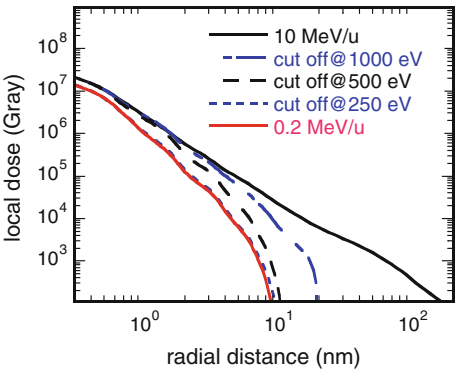

Fig. 2.8 Evolution of the radial distribution of the dose as function of cut-off energy, $E_{cut\text{-}off}$, of primary electrons for a beam energy of 10 MeV/u Kr in mica. The *red line* shows the evolution of the radial dose for 0.2 MeV/u without any cut-off. Figure extracted from Bouffard et al. [25]

Since the track radius R_t is in the order of 5 nm the dose deposited at larger distance ($r > R_t$) is not efficient to create a track. Consequently, only electrons having energy lower than the so-called cut-off energy $E_{cut\text{-}off}$ will be considered. The evolution of the radial dose distribution for Kr irradiation in mica is plotted as function of the radial distance r for several values of this cut-off energy in Fig. 2.8, showing that it becomes efficient for $T_{cut\text{-}off} \leq 1000$ eV. It is shown that for a cut-off energy of 250 eV the local dose distribution for 10 MeV/u Kr ions becomes the same as that for 0.2 MeV/u. Such an agreement is the result of neglecting the dose given to the atoms by electrons with energy larger than 250 eV.

The reduced energy loss $S_{e\text{-}red}$ is then calculated (Fig. 2.7b) using (2.1) [3], with E_{em} replaced by $E_{cut\text{-}off}$.

$$S_{e-red} = -\left(\frac{dE}{dx}\right)_{red} = N \int_0^{E_{cut-off}} E_e \sigma(E_i, E_e) dE_e \tag{2.5}$$

where $\sigma(E_i,E_e)$ is the differential cross section for electron emission. Independent of the cut-off energy, between 100 and 500 eV the dose distribution remains nearly unchanged (Fig. 2.8). By choosing $E_{cut\text{-}off}$ = 200 eV, the track radii versus the reduced electronic energy loss lie on the same curve for all ion energies (Fig. 2.7b). So, the difference in radii between high and low beam energies (Fig. 2.7a) disappears if only the energy which is deposited near the ion path is considered instead of the total electronic energy loss.

This model developed by Bouffard et al. has been proposed as a possible model to predict the experimental track radii directly from the initial energy deposition of the electrons as obtained by Monte Carlo calculation without any other radial expansion of the initial energy. It is disappointing that, to our knowledge, this model up to now was applied only for mica.

2.3.5 A Transient Thermal Process

The thermal spike was proposed by Desauer [95] and reconsidered for insulators by Chadderton and Montagu-Pollock [96] and for metals by Seitz and Koehler [97]. The main idea of this model is to suppose that the energy deposited in the lattice can be described by a transient thermal process acting in the electronic and atomic subsystems. We denote it more specifically as the inelastic thermal spike (i-TS) model [44–51] to emphasize the difference with the elastic collision spike model which is valid in the nuclear energy loss regime [98]. In the i–TS model, the energy deposited in the electrons by the slowing down of the incident ions diffuses within the electron subsystem by electron-electron interactions before being transferred and finally localized in the lattice system via the electron–phonon coupling. The heat diffusion in the electron and in the lattice subsystems versus time t and space r (in cylindrical geometry) is described by the following two coupled differential equations [99]:

$$C_e(T_e)\frac{\partial T_e}{\partial \mathrm{t}} = \frac{1}{r}\frac{\partial}{\partial r}\left[rK_e(T_e)\frac{\partial T_e}{\partial r}\right] - g(T_e - T_a) + A(r) \tag{2.6}$$

$$C_a(T_a)\frac{\partial T_a}{\partial t} = \frac{1}{r}\frac{\partial}{\partial r}\left[rK_a(T_a)\frac{\partial T_a}{\partial r}\right] + g(T_e - T_a) \tag{2.7}$$

where $T_{e,a}(r,t)$, $C_{e,a}(r,t)$ and $K_{e,a}(r,t)$ are the temperature, the heat capacity per unit volume (called specific heat in the following) and the thermal conductivity of the electronic (e) and atomic (a) subsystem, respectively. $A(r)$ is the energy deposited into the electronic system [26]. The only free parameter in this model is the electron–phonon coupling strength g [55].

At present different ways exist to explore the heat diffusion equations for describing the occurring physical processes and calculating experimentally accessible quantities:

I The so-called analytical thermal spike (a-TS) model proposed by Szenes [41, 42] provides an analytical solution of the differential equation for the atomic system (2.7) ignoring the way the energy is transferred to the atoms. This model was extended by Trinkaus [58] to describe the anisotropic growth in amorphous materials under swift heavy ion irradiation (see Chap. 10).

II The ionization diffusion-explosion-amorphization (IDEA) model by Canut and Ramos [43] takes into account the energy diffusion to the electrons prior to its transfer to the atoms by providing an analytical solution of the differential equation for the electronic system (2.6).

III In the inelastic thermal spike (i-TS) model [44–51] a complete numerical solution of the system of differential equations [(2.6) and (2.7)] is given taking into account the coupling between the electronic and atomic subsystems.

IV Finally, in the exciton decay model [38] it is assumed that the energy delivered by the thermal spike leads to the formation of bound excitons. Their nonradiative decay results in the creation of point defects.

The different approaches mentioned will be discussed in the following subsections taking into account the energy criterion to create a track that will change with the model proposed.

2.3.5.1 The Analytical Thermal Spike (a-TS) Model

Within the analytical thermal spike (a-TS) model [41, 42, 100] the various ion-induced physical effects are determined by the maximum temperature, and the actual time evolution of the temperature spike is not considered. It is assumed that the ion-induced temperature increase $\Delta T(r,t)$ can be approximated by a Gaussian distribution function, which is an analytical solution of (2.7):

$$\Delta T(r,t) = \gamma S_e / \pi \rho c a^2(t) e^{-(r^2/a^2(t))} \tag{2.8}$$

where ρ and c are the density and the heat capacity, γS_e is the fraction of S_e deposited in the thermal spike with an efficiency of γ and $a(t) = a(0) + 4Dt$ where $a(0)$ is the initial width of the radial distribution of the temperature approximated by a Gaussian function in the phonon system, Dt is the squared value of energy diffusion length versus time of the considered material with a thermal diffusivity D. Szenes [41] had assumed that the maximum track size is reached at $t = 0$, and $\Delta T(r,0)$ is calculated only with $a(0)$.

A typical temperature distribution is plotted versus the radius for $Y_3Fe_5O_{12}$ in Fig. 2.9. The track radius R_m in $Y_3Fe_5O_{12}$ can be found using the temperature distribution defined at time $t = 0$,

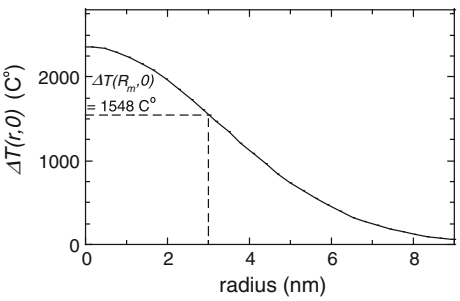

Fig. 2.9 Radial temperature distribution for $Y_3Fe_5O_{12}$, irradiated with an ion energy of 1 MeV/u and with S_e = 10 keV nm^{-1}. $\Delta T(r,0) = 2350 \exp(-r^2/a(0)^2)$ with $\gamma = 0.35$, ρ = 5.18 g cm^{-3}, c = 0.68 J K^{-1} cm^{-3} and $a(0)^2$ = 21.6 nm^2 [41, 42]. At the melting temperature $\Delta T(R_m,0)$, the radius is equal to 2.9 nm in agreement with that measured by Meftah et al. [18]

$$\Delta T(R_m, 0) = T_0 = T_m - T_{ir} \tag{2.9}$$

where T_{ir} (usually 300 K) is the irradiation temperature and T_m = 1848 K the melting temperature. Here the energy needed to make the solid to liquid phase change is ignored. Such assumption is surprising since it has been shown by Rethfeld et al. [101] that the shorter the energy deposition time the larger is the temperature to melt the material. But it is presumed in this model that the electronic energy deposition induces a decrease of the bonding strength in the irradiated material as it was proposed by Van Vechten et al. [39] (see Sect. 2.3.2 in this chapter). The two free parameters of the model are the fraction γ of S_e deposited in the atoms, and $a(0)$ the initial Gaussian width.

Under these assumptions, two simple equations for the track radius R can be derived from (2.8):

$$R^2 = a^2(0)\ln(\mathrm{S_e}/\mathrm{S_{et}}) \text{ for } \mathrm{S_e} < 2.7\,\mathrm{S_{et}} \tag{2.10}$$

$$R^2 = (a^2(0)S_e)/(2.7S_{et}) \text{ for } S_e > 2.7\,\mathrm{S_{et}} \tag{2.11}$$

where S_{et} is the electronic energy loss threshold for track formation. This threshold is the most important parameter and can be deduced either by fitting the track radii near the threshold [41, 42] using (2.10) or directly by plotting the damage cross section σ, which can be calculated from experimentally determined track radii, versus the electronic energy deposition S_e. The extrapolation of the resulting $\sigma(S_e)$ curve then yields the threshold value S_{et} [27] (see also Chap. 9). $a(0)$ can also be deduced from (2.10) and (2.11) since it is equal to the measured radius for S_e = 2.7 S_{et}. Knowing S_{et} and $a(0)$, track radii can be fitted. In the a-TS model, the criteria for track formation are on one hand the energy to reach the melting temperature and on the other hand the fraction γ of S_e which is deposited to the atoms to create a track. The efficiency γ is given by

$$S_{et} = (\pi\rho c T_0 a^2(0))/\gamma \tag{2.12}$$

if $a(0)$ is known or, by substituting $a^2(0)$ from (2.11) in (2.12), can be determined according to

$$\gamma = 2.7\pi\rho c T_0 R^2/S_e. \tag{2.13}$$

According to Szenes, the most important features of the a-TS model are that the initial Gaussian width is uniformly $a(0)$ = 4.5 nm and that the efficiency is $\gamma \sim 0.4$ at low and $\gamma \sim 0.17$ at high ion velocities, respectively. Thus there is no free parameter characteristic for various insulators at low and high ion velocities in this model (for details see [41, 42]).

The a-TS model, first developed for insulators [41, 42], was extended to polymers [102], to biological samples [103], as well as to materials with highly anisotropic electrical conduction [104].

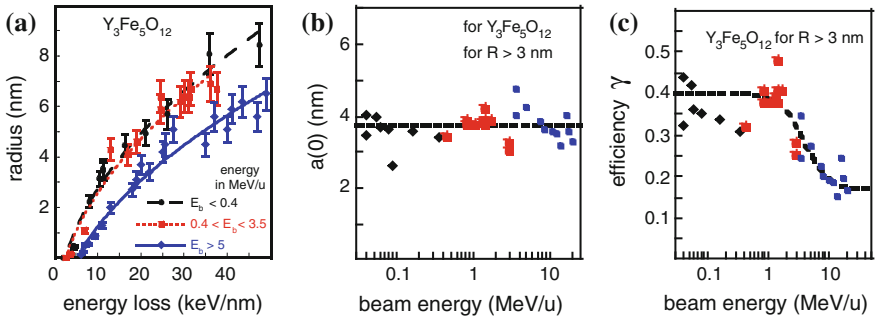

Fig. 2.10 **a** Experimental track radius versus electronic energy loss in $Y_3Fe_5O_{12}$ for three different ranges of beam energy (the lines are square root fits of the experimental radii for the corresponding beam energy; figure extracted from Toulemonde et al. [109]). **b** Evolution of a(0) versus beam energy from (2.11). **c** Evolution of the efficiency versus beam energy (figure extracted from Szenes [41, 42] from 2.12 and 2.13. For (**b**) and (**c**), the lines are there to guide the eyes

In order to illustrate the determination of $a(0)$ and γ, the measured track radii of $Y_3Fe_5O_{12}$ for which track formation is extensively studied [18, 105–107], will be analyzed in more detail. The measured radii are plotted in Fig. 2.10a for various groups of beam energies E_b versus the electronic energy deposition. By extrapolation to the radius $R = 0$, the threshold values of the electronic energy deposition are $S_{et} = 4$ keV nm^{-1} for $E_b < 3.5$ MeV/u and 7 keV nm^{-1} for $E_b > 5$ MeV/u (from Fig. 2.13 in [18]). Then the measured R values at $2.7 \times S_{et}$ are ~ 3 nm whatever the beam energy is (Fig. 2.10a). In order to verify such $a(0)$ determination the width is calculated using (2.11) for experimental radii > 3 nm with the corresponding S_e values in Fig. 2.10a. In these cases continuous tracks are formed in $Y_3Fe_5O_{12}$ [107].

The result leads to a mean value of $a(0) = 3.8 \pm 0.4$ nm independent of the beam energy. This value is larger than the value of 3 nm determined from $S_e = 2.7 \times S_{et}$ but lower than the mean value of 4.5 nm deduced by Szenes from the analysis of track data in several materials ($Y_3Fe_5O_{12}$, $BaFe_{12}O_{19}$, $SrFe_{12}O_{19}$, $MgFe_2O_4$, $NiFe_2O_4$, and $ZnFe_2O_4$) [41, 42]. The experimental values of the radii at low (Fig. 2.11a) and high ion energies (Fig. 2.11b) are compared with the description in the framework of the Szenes model using three values of $a(0)$: 3, 3.8 and 4.5 nm. The results confirm that the value $a(0) = 3.8$ nm seems to give the best agreement with the experimental data for ion energies below ~ 3.5 MeV/u (Fig. 2.11a), whereas for energies of ~ 15 MeV/u the best agreement is reached for $a(0)$ between 3.8 and 5.0 nm (Fig. 2.11b), surrounding the 4.5 nm deduced by Szenes. With (2.13), it is possible to calculate the efficiency γ for the track radii larger than 3.0 nm for all the beam energies using $\rho = 5.15$ g cm^{-3}, $c = 0.68$ J g^{-1} K^{-1} and $T_m = 1848$ K. This leads to $\gamma = A\ R^2/S_e$, with $A = 2.7\pi rcT_0 = 0.29$ keV nm^{-3}, which is plotted versus the beam energy in Fig. 2.10c. Three regimes may be defined: for $E_b < 2$ MeV/u, γ is constant and equal to 0.4, then for E_b between 2 and 10 MeV/u there is a transition regime with γ decreasing smoothly from 0.4 to 0.17

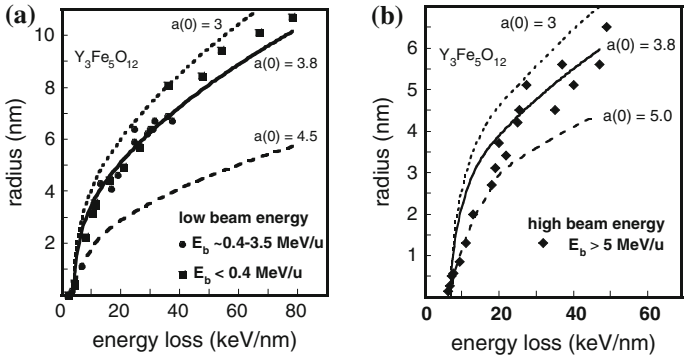

Fig. 2.11 Experimental radii versus electronic energy loss for $Y_3Fe_5O_{12}$ irradiated with various ion energies compared to radii calculated in the ATS model using different values of the initial width a(0) in nm. **a** For beam energy less than 3.5 MeV/u, using S_{et} = 4 keV nm^{-1} [18, 106] and **b** for beam energy ~15 MeV/u, using S_{et} = 7 keV nm^{-1} [17]

and afterwards, for energies larger than 10 MeV/u, γ seems to stay constant and equal to 0.17. This is in agreement with the velocity effect [18] since the energy density deposited in the atoms decreases with beam energy.

Using the model of Szenes [41], Moll et al. [108] analyzed the measured radii in pyrochlores ($Gd_2Ti_{2-x}Zr_xO_7$ for x = 0, 1 and 2) which have been irradiated with ions at energies between 10 and 6.5 MeV/u. Since the experimental electronic energy loss threshold for track formation is $S_{et} \sim 13$ keV nm^{-1} (Fig. 2.12) for each material, the track radii belong to an electronic energy loss range below $S_e = 2.7 \times S_{et} = 35$ keV nm^{-1} and the radii are fitted using the square root of (2.10). The best fits to the data (Fig. 2.12) provide the following values of the parameters: $a(0) = 5.8$ nm and $S_{et} = 13.2$ keV nm^{-1} leading to $\gamma = 0.32$ for $Gd_2Ti_2O_7$, $a(0) = 4.9$ nm and $S_{et} = 13.2$ keV nm^{-1} leading to $\gamma = 0.26$ for

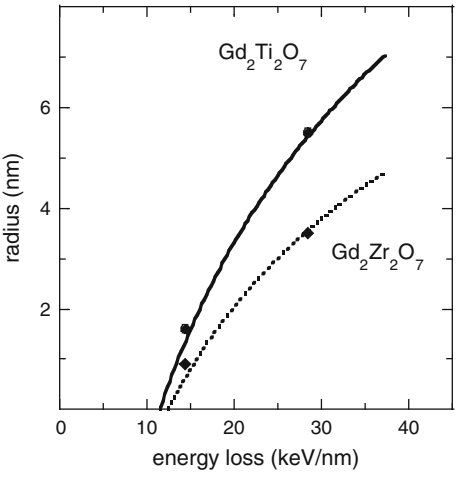

Fig. 2.12 Variation of the radius R as a function of the electronic energy loss, S_e, in pyrochlore samples irradiated with Kr and Xe at energies larger than 6.5 MeV/u. The lines are fits to the data in the framework of the model of Szenes (data extracted from Moll et al. [108]) (for $Gd_2Ti_2O_7$: S_{et} = 13.2 keV nm^{-1} and a(0) = 4.9 nm, and for $Gd_2Zr_2O_7$: S_{et} = 13.8 keV nm^{-1} and a(0) = 4.1 nm)

Gd_2TiZrO_7 and $a(0)$ = 4.1 nm and S_{et} = 13.8 keV nm^{-1} leading to γ = 0.20 for $Gd_2Zr_2O_7$. It should be noted that $a(0)$ varies from 5.8 to 4.1 nm which encircles the value of 4.5 nm determined by Szenes as observed for the high energy regime in $Y_3Fe_5O_{12}$ (Fig. 2.11b). The efficiency γ is varying from 0.32 to 0.20. This is not expected since the efficiency should be smaller than 0.2 for beam energies larger than 6 MeV/u (Fig. 2.10c) according to the model of Szenes [41, 42].

Consequently, the a-TS model gives a quantitative description of track radii in insulating materials provided that the Gaussian width $a(0)$ at time $t = 0$ can be deduced from the knowledge of the threshold value S_{et} for track formation ($a(0)$ equals the track radius at $S_e = 2.7\ S_{et}$) as well as from the track size for S_e larger than 2.7 S_{et} for a specific beam energy. The efficiency γ, with the knowledge of $a(0)$ [(2.11) and (2.12)], determines the fraction of S_e deposited in the track. It does not take into account the latent heat energy needed for the phase change from solid to liquid which is based on the assumption that for track formation the melting temperature of the corresponding material is exceeded. However, with the knowledge of $a(0)$ and γ, this model provides an initial temperature distribution of the atomic system. This has been successfully used by Klaumünzer [30] to describe the anisotropic growth in amorphous silica, using γ = 0.6.

2.3.5.2 The Ionization Diffusion-Explosion-Amorphization (IDEA) Model

In the model developed by Canut and Ramos [43], it is assumed that the damage evolution via collective electronic excitations takes place in four steps. The model takes into account the energy deposition in the electrons by an analytical solution of (2.6) governing the energy diffusion to the electrons.

(1) The first stage concerns the interaction of the incident ions with the electrons of the lattice. The resulting ionization process is caused by the energy density $A(r)$ initially deposited in the electronic system [26] (see Sect. 2.2.2).
(2) The energy density W initially deposited in the electrons diffuses via electron-electron collisions before its transfer to the lattice according to

$$\frac{\partial W(r,t)}{\partial t} = \frac{D}{r}\frac{\partial}{\partial r}\left[r\frac{\partial W(r,t)}{\partial r}\right] + A(r) \tag{2.14}$$

After the diffusion process has finished, the final energy density profile will be given by $W_1(r) = W(r, \tau)$ at a time τ. By integration of (2.14), $W_1(r)$ is obtained,

$$W_1(r) = \frac{1}{2D\tau}\int_0^{r_m} uW_0(u)I_0\left(\frac{ru}{2D\tau}\right)e^{-\frac{r^2+u^2}{4D\tau}}du \tag{2.15}$$

where I_0 is the zero order hyperbolic Bessel function, τ is the duration of the diffusion process, D the energy diffusivity of the electrons and r_m is the

maximum radius of the energy distribution ($W(r, 0) = 0$ *for* $r > r_m$). τ should be in the order of the phonon period $\sim 10^{-12}$ s, and the diffusion length L_d characteristic for the material is defined by $L_d^2 = 2D\tau$. The integration of (2.15) is described in detail in [43].

(3) At the end of the diffusion stage the energy is transferred to the atomic system, in analogy with an explosion mechanism, if $W_1(r)$ exceeds a critical density W_c at the radius $r = r_1$. Here it is assumed that the part of the $W_1(r)$ distribution below W_c ($r > r_1$) does not create irreversible atomic disorder. Therefore an effective electronic stopping power S_e^* which represents the energy per unit length deposited in this "hot" region is defined according to

$$S_e^* = \int_0^{r_1} 2\pi r W_1(r) dr \tag{2.16}$$

(4) In this stage an equipartition of energy above W_c is assumed resulting in an extension of the cylinder where energy deposition occurs from r_1 to a final value r_e, the effective radius of the track. That means that the atoms excited within r_1 share their energy with atoms in the larger radius r_e. At the end of this amorphization process the radial density of deposited energy $W_e(r)$ inside the track is equal to the critical energy density $W_c = W_1(r_1)$ leading to a cross section $\sigma = S_e^*/W_c$.

The model was successfully applied to $LiNbO_3$ [43] and $Y_3Fe_{15}O_{12}$ [109, 110]. As example, in the following the application of the model to $Y_3Fe_{15}O_{12}$ irradiated with cluster and single ions will be briefly described.

Using cluster ion irradiation with its very low particle velocity (~ 0.05 MeV/u) and very high electronic energy loss, the kinetic energy given to electrons by ion-electron collisions is very low and consequently the initial energy deposition can be approximated by a Dirac distribution. In that case, (2.15) may be approximated by

$$W_1(r) = \frac{S_e}{2\pi L_d^2} e^{(-r^2/2L_d^2)} \tag{2.17}$$

Using (2.16) with the assumption that $W_c = W_1(r_1)$, the effective electronic energy loss S_e^* is linked to S_e by the relation $S_e^* = S_e - 2\pi L_d^2 W_c$. Knowing that the damage cross section $\sigma = S_e^*/W_c = S_e/W_c - 2\pi 2L_d^2$, with the use of the last relation W_c and L_d can be determined by fitting the track radius r assuming that $\sigma = \pi r^2$.

The damage cross sections resulting from the cluster irradiations of $Y_3Fe_5O_{12}$ are plotted versus electronic energy loss in Fig. 2.13a. The values of W_c and L_d equal to 20 keV nm^{-3} and 1.7 nm, respectively, are extracted from a fit of the damage cross sections. With these values of W_c and L_d the effective electronic energy loss S_e^* is calculated. In Fig. 2.13b the experimental values of track radii for

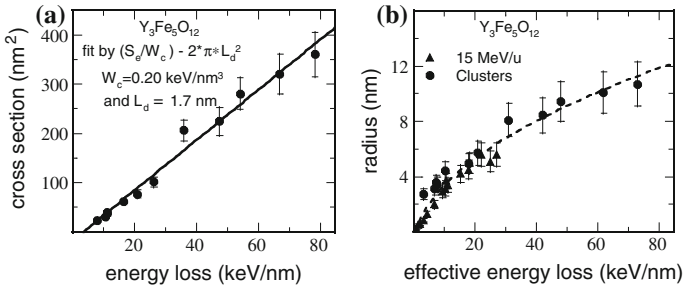

Fig. 2.13 **a** Damage cross section in $Y_3Fe_5O_{12}$, irradiated by cluster beams [109] versus electronic energy loss; **b** Track radii [18] versus effective electronic energy loss resulting from cluster beams and ions at 15 MeV/u

cluster and 15 MeV/u ion irradiations are plotted versus the effective energy loss. As can be seen the radii for both irradiation regimes are in good agreement.

2.3.5.3 The Inelastic Thermal Spike (i-TS) Model: A Complete Numerical Solution of the Heat Diffusion Equations

The common features of the i-TS model for metallic or insulating materials are the following [27, 44–51]:

a. The input energy of the spike is the known electronic energy loss described by the radial and time distribution function $A(r, t)$ obtained by Monte Carlo Calculations [26] for a specific beam energy (see Sect. 2.2.2).
b. The heat diffusion in the electron and lattice subsystems are described by coupled Fourier equations. Since the electronic energy deposition can be considered as constant along the trajectory, the heat equations are solved in a cylindrical geometry. The deposited energy and its evolution are deduced from a numerical solution of (2.6) and (2.7) allowing the calculations of the energy transfers to electronic and atomic subsystems, respectively. The initial boundary conditions of the calculations are first the temperature (T_0) of the irradiated lattice or the equivalent internal energy, $E_i(T_0)$, and the volume in which the calculations are performed. From the initial temperature of irradiation, T_0, the internal energy is calculated by an integration of the specific heat from 0 K to T_0. The distance that defines the volume in which the calculation is performed should be sufficiently large to be sure that the temperature gradient is negligible far away from the centre of the trajectory (usually a cylinder radius of $\sim$200 nm). The evolution of the electronic and atomic temperature around the projectile trajectory is calculated as a function of time t and space r. This is illustrated in Fig. 2.14 for the case of an irradiation of pure Fe (T_0 = 80 K and $E_i(T_0)$ = 0.002 eV/at) which shows the temperatures of electronic $T_e(t,r)$

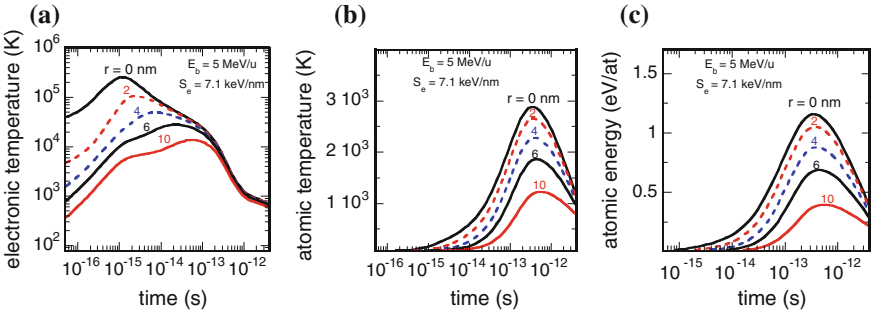

Fig. 2.14 Electronic (**a**) and atomic (**b**) temperature and energy transferred to the atoms (**c**) versus time for different radial distances in nm from the ion path. This calculation is performed for pure Fe irradiated at 80 K with an U beam of 5 MeV/u with $g = 1.2 \times 10^{12}$ W cm^{-3}K^{-1} and $S_e = 71$ keV nm^{-1} [76]

(Fig. 2.14a) and atomic systems $T_a(t,r)$ (Fig. 2.14b) versus the time for different distances from the centre of the ion trajectory.

c. It is assumed that the relaxation of the excited electron system proceeds via electron-electron and electron-atom collisions characterized by the electron-phonon coupling strength g [55, 99]. This is connected with the electron-phonon mean free time $\tau = C_e(T_e)/g$ and with the electron-phonon mean free path $\lambda^2 = D_e\ (T_e) \times \tau = K_e(T_e)/g$ where $C_e(T_e)$ and $K_e(T_e)$ are the specific heat and the thermal conductivity, respectively, for the electronic (e) subsystem at an electronic temperature T_e [44, 48, 50].

d. Due to the short heating rate of the atoms the equilibrium melting temperature T_m is not the adequate parameter to characterize the melting process. This was experimentally observed with femtosecond laser experiments [111], i.e. the measured increase of temperature versus the input laser power does not stop at T_m but continues to increase above T_m. This was also shown by Rethfeld et al. [101]: the temperature allowing the nucleation of a molten phase is larger than T_m by a factor of ~ 1.3 when the heating rate is in the order of 10^{15} K s^{-1}. Such effect was also pointed out by Klaumünzer [30], and in [112] it was shown that the superheating melting temperature is in the order of 500 K larger than T_m if the heating rate is in the order of 10^{14} K s^{-1} [112]. In the case of Fe, the heating time to reach T_m (1809 K) is $\sim 10^{-13}$ s, leading to a heating rate of $\sim 10^{16}$ K s^{-1} (Fig. 2.14b). So the calculations were made within a superheating scenario, i.e. the increase of temperature does not stop at the melting or vaporization temperature. Such hypothesis was systematically used after 2002 [113, 114] and as an example the evolution of $T_a(r,t)$ is plotted versus time for pure Fe in Fig. 2.14b. Using the relation $E_a(r,t) \sim \int_0^{T_a(r,t)} C_a(T_a(r,t))dT_a$, the evolution of the energy $E_a(r, t)$ transferred to the atoms is plotted in Fig. 2.14c versus time t for different radii r where $C_a(T_a(r, t))$ is the specific heat of the lattice at $T_a(r, t)$. Within this superheating scenario the temperature in Fig. 2.14b

does not have the usual meaning and should be taken only as an equivalent energy transferred to the atoms.

e. Taking into account the superheating scenario, the energy E_m necessary to reach the molten phase is defined as the energy to reach the melting temperature T_m plus the latent heat of fusion [44]. Using the same criterion the track size is defined by the largest radial zone of the atoms which contains sufficient energy $E > E_m$ to induce the molten phase. In the case of pure Fe, the energy to create a track is 0.86 eV/at while the energy corresponding to the melting temperature (T_m = 1809 K [50]) is equal to 0.70 eV/at $(E_a(T_m) \sim \int_0^{T_m} C_a(T_a)dT_a)$, i.e. 0.16 eV/at smaller than the energy to reach the energy necessary for melting. The equivalent superheating temperature to create a track is then 2156 K, i.e. 347 K larger than the melting temperature as expected from the rapid heating rate.

f. For the thermophysical parameters (thermal conductivity, specific heat, melting temperature, heat of fusion, boiling temperature, heat of evaporation) the equilibrium values are used even within the transient conditions of the spike. If the latent heat of fusion is unknown, then the track radii were fitted with a unique couple of values, g or λ, with the corresponding E_m, for a metallic material a-$Fe_{85}B_{15}$ [115], a semiconductor GeS [116] and an insulator $Gd_2Ti_2O_7$ [117] as examples.

Application of the i-TS Model to Metallic Materials: Amorphous Versus Crystalline Materials

The inelastic thermal spike process was developed by Dufour et al. for Bi [48] and compared to other metallic materials by Wang et al. [50]. The first attempt to apply the model was performed for amorphous materials [29, 45] supported by the idea that the electron-phonon coupling in amorphous metallic alloys is larger than in crystalline ones.

The two coupled diffusion equations [(2.6) and (2.7)] were solved numerically [51] by taking into account the evolution of all parameters with the temperature. For the energy diffusion to the electrons, the electronic specific heat (C_e) and the electronic thermal conductivity (K_e) were calculated using the formalism of the free electron gas model [48]. Regarding the energy diffusion to the atoms the measured specific heat and the atomic thermal conductivity versus atomic temperature were introduced.

The electron-phonon coupling strength g is the key parameter governing the rate of the electron energy relaxation towards the lattice [118]. A relation for the electron-phonon coupling efficiency has been developed for metallic materials, and for a complete derivation we refer to the work of Brorson et al. [119] and Allen [120]. If the temperature of the electronic system is higher than the Debye temperature, $T_e > T_D$, then Kaganov et al. [55, 99] obtain

$$g(T_e) = \frac{\left(\frac{\pi^2}{6}\right) m_e n_e v_s^2}{\tau(T_e) T_e}. \tag{2.18}$$

n_e and m_e are the electronic density and the free electron mass, respectively, v_s is the sound velocity which writes $v_s = 2\pi k_B T_d/(h6\pi^2 n_a)$ where n_a is the atomic density, k_B is the Boltzmann constant, T_D the Debye temperature and h the Planck constant. With the Wiedemann-Franz law giving the connection between electronic and thermal conductivity, $K_e(T_e) = L^* \sigma_e(T_e) T_e$, with $L^* = (\pi^2 k_B^2)/(3e^4)$ the Lorentz number, $g(T_e)$ is expressed as

$$g(T_e) = \frac{\pi^4}{18} \frac{1}{(6\pi^2)^{2/3}} \frac{1}{n_a^{2/3}} \frac{(n_e e T_D)^2}{K_e(T_e)}. \tag{2.19}$$

It is obvious in (2.19) that $g(T_e)$ is inversely proportional to the thermal conductivity $K_e(T_e)$, which is illustrated in Fig. 2.15 for pure iron. Since in metals the thermal conductivity behaves identical with temperature as the electrical conductivity, $g(T_e)$ is also proportional to the reciprocal of the electrical conductivity. If the temperature of the electronic system becomes smaller than that of the atomic system, $T_e < T_a$, then in metallic systems the atoms are cooled by energy exchange with the electrons [48]. This leads to an atomic cooling rate of the order of the heating rate. However, the electron-phonon coupling strength is not well known and consequently it is considered as a free parameter and is determined by fitting

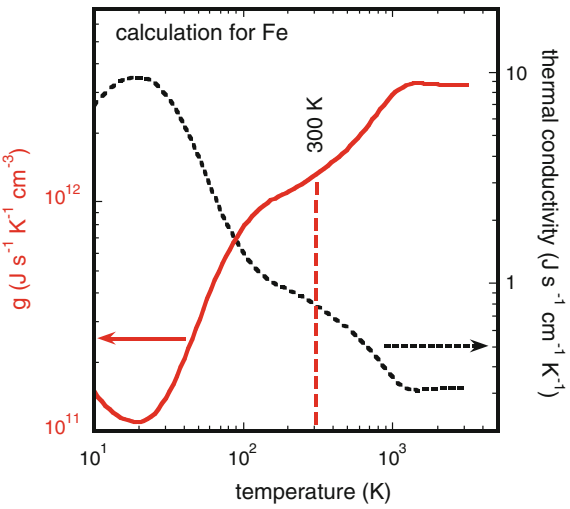

Fig. 2.15 Thermal conductivity (*dotted line* and unit on the *right*) and electron-phonon coupling strength, g (*red line*), versus atomic temperature for pure iron. At 300 K, g = 1.3 × 10^{12} J s^{-1} K^{-1} cm^{-3} [55, 99]

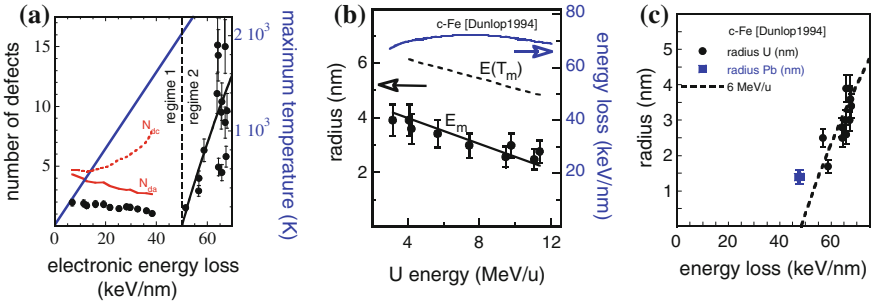

Fig. 2.16 **a** Number of defects [76] in Fe versus electronic energy loss compared to calculations with the i-TS model. *Regime 1*: defect annealing, *regime 2*: defect creation. N_{dc} is the number of defects calculated by SRIM and N_{da} is the number of stable defects calculated with the i-TS model after annealing by the electronic energy loss. **b** Radii and electronic energy loss versus the U ion energy. Calculations with the i-TS model have been performed using two different criteria: first with the energy to reach the melting temperature $E(T_m)$, and second with the energy to reach the melting phase, E_m [109]. **c** Experimental track radii for U and Pb irradiated Fe versus the electronic energy loss compared with values calculated with the i-TS model for ions of $\sim$6 MeV/u

the track size. The g values determined in this way usually well agree with the predictions of (2.19) in the case of metallic materials apart for Ti [50].

A typical case for track observation in a metallic material is the irradiation of pure iron [76]. The defect creation by high electronic excitations was quantified by resistivity measurements directly correlated with the number of created defects inside the metallic material. In Fig. 2.16a, the number of defects created in Fe is plotted versus the electronic energy loss. Concerning the effect of the electronic energy deposition on structural modification in Fe, two regimes can be distinguished: first a decrease of the number of defects below 50 keV nm^{-1}, second an increase of defect creation above this energy loss.

In the first regime, below 50 keV nm^{-1}, the measured number of defects N_d (black dots in Fig. 2.16a) decreases with the electronic energy loss due to ionization induced annealing. In the same region of electronic energy deposition the defect concentration N_{dc} calculated by SRIM [14] increases (see dotted red curve in Fig. 2.16a). Assuming that the annealing of the defects is thermally activated [121], the number of residual defects N_{da} (solid red curve in Fig. 2.16a) along the ion path is calculated using the thermal spike model [122], assuming an electron-phonon coupling strength of $g = 1.3 \times 10^{12}$ J s^{-1} cm^3 K^{-1} for Fe at 300 K. This value is quite in agreement with 1.2×10^{12} J s^{-1} cm^3 K^{-1} obtained from (2.19) [50]. N_{da} decreases as also experimentally observed (compare solid red curve and black dots in Fig. 2.16a). The calculated larger values of N_{da} as compared to the experimental points are due to the fact that non thermal annealing or defect recombination in the nuclear cascade is not taken into account in the calculations. The maximum temperature of the atomic system reached along the ion track is also plotted versus the electronic energy loss in Fig. 2.16a, showing that the melting temperature (1809 K) is exceeded above 50 keV nm^{-1}.

Above 50 keV nm^{-1} an increase of the defect concentration with increasing electronic energy deposition is observed (black dots in Fig. 2.16a). This second regime can therefore be attributed to defect creation by electronic excitations. It can be assumed that melting of the material around the ion trajectory and subsequent resolidification lead to defect production in a cylinder with a radius which can be obtained from the damage cross section σ [76]. It is assumed that $\sigma = \pi R^2$ where R is the track radius. The energy to create a track was deduced by fitting the track radius measured after an irradiation of Fe by U ions. Two calculations were performed using the g value previously determined from the description of the defect annealing for $S_e < 50$ keV nm^{-1}: In a first scenario the cylinder radius calculated with the energy $E(T_m)$ necessary to reach the melting temperature T_m which is equal to 0.70 eV/at yields an overestimation of the calculated radii compared to the experimental values (Fig. 2.16b). The second calculation assumed an energy to create a track equal to $E_m = E_a(T_m) + H_m = 0.86$ eV/at where H_m is the energy to make the solid to liquid phase transition. Within this last hypothesis the calculated cylinder radii agree with the experiment (Fig. 2.16b). This supports that the equilibrium melting temperature is not an adequate criterion to describe track formation. An energy of 0.86 eV/at corresponds to an effective temperature T_{eff} equal to 2156 K which is larger than T_m as suggested [101, 112]. The track radii calculated with the same electron phonon coupling strength ($g = 1.2 \times 10^{12}$ J s^{-1} cm^{-3} K^{-1}) for an ion energy of 6 MeV/u are in good agreement with the experimental values, as it can be seen in Fig. 2.16c.

Applying this model to Bi the measured radii versus electronic energy loss can be described by using an electron-phonon coupling strength [48] equal to 4×10^{11} J s^{-1} cm^{-3} K^{-1} (see Chap. 8) with $E_m = 0.26$ eV/at. Moreover in this material a temperature effect was observed [123]: the higher the temperature the larger is the track size.

Tracks in the metallic glass a-$Fe_{85}B_{15}$ were also detected by means of SAXS (Small Angle X-ray Scattering) measurements [115]. For these investigations a-$Fe_{85}B_{15}$ was chosen because the track size had been already determined by means of ion fluence dependent resistivity measurements [124–126]. A comparison of the radii determined with different physical characterization methods in Fig. 2.17

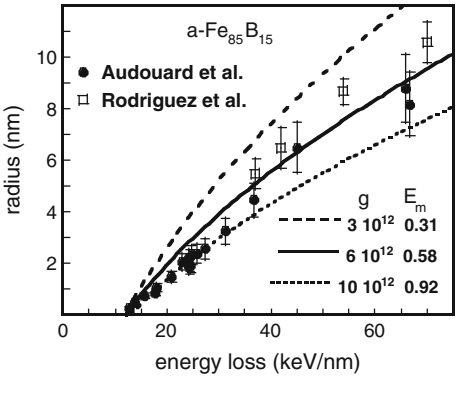

Fig. 2.17 Track radii versus electronic energy loss obtained from resistivity (*full circles* [124]) and SAXS measurements (*open squares* [115]). The lines are i-TS calculations with the parameters g (in W cm^{-3} K^{-1}) and E_m (in eV/at) given in the figure

(measurement points) shows very good agreement. For determining track radii in the framework of the i-TS model, beside other parameters the knowledge of the electron-phonon coupling strength, g, and the energy necessary to melt the material, E_m, are needed. The latter are unknown for the metallic alloys. Merely with the measured melting temperature $T_m = 1496$ K for a-$Fe_{85}B_{15}$ [127] the energy $E_m = 0.31$ eV/at could be evaluated. Therefore several calculations were performed with values of $g = 3 \times 10^{12}$, 6×10^{12} and 10×10^{12} W cm^{-3} K^{-1} in order to determine E_m by fitting the electronic energy loss threshold of $\sim$13 keV nm^{-1}. The corresponding energies to melt are $E_m = 0.31$, 0.58 and 0.92 eV/at respectively. The radii calculated with these parameters are compared with the experimental results in Fig. 2.17. As can be seen, the experimental values of the evolution of the track size as function of the electronic energy deposition, S_e, are best described with $g = 6 \times 10^{12}$ W cm^{-3} K^{-1} and $E_m = (0.58 \pm 0.06)$ eV/at. In comparison to pure Fe, the electron-phonon coupling strength, g, is larger and the energy to melt, E_m, is smaller in this alloy. Such deviation of the parameters agrees with the decrease of the electrical conductivity of an amorphous metallic alloy compared to the crystalline phase and to the decrease of the energy to reach the molten phase in an amorphous material, respectively [29].

It should be mentioned that with the model developed by Trinkaus et al. [58, 59] the anisotropic growth of amorphous metals [128] and insulators [30, 129–131] under swift heavy ion irradiation can be successfully described assuming an effective temperature of melting T^*. This anisotropic growth results from the appearance of a molten track along the ion path. This phenomenon is described in more detail in Chap. 10.

Materials with Bonded Electrons: Insulators and Semiconductors

(A) *Description of track size, sputtering yield, ion velocity effect.*

The way how the high energy of the electronic system induced by swift heavy ions is transferred to the lattice atoms of an insulator is described by Baranov et al. [132]: hot electrons are excited in the conduction band and then behave like hot electrons in metals and cool down by excitations of electrons from the valence band to the conduction band and by transferring their energy to the atoms. Such concept was recently revised [133, 134] showing that crystalline SiO_2 irradiated by swift heavy ions undergoes a large enhancement of the electrical conductivity comparable to that of metals like gold, supporting the first step of this schematic description. But the values of the electron-phonon coupling strength are unknown for insulators in the case of high electronic excitations. Consequently, instead of g as the free parameter, the electron-phonon mean free path λ, which is defined as $\lambda^2 = D_e C_e / g$ (Sect. 2.3.5.3c) with $D_e = 2$ cm^2 s^{-1} and $C_e = 1$ J cm^{-3} K^{-1} corresponding in first approximation to the values for hot electrons in metals is used. Moreover, in the case of insulators the energy exchange from the atoms to electrons is inhibited and the atomic cooling rate, characterized by the thermal diffusivity of

the atoms [44], is one order of magnitude smaller than the heating rate. To illustrate the application of this model to insulators, three materials will be analysed: (1) SiO_2 quartz in its crystalline phase where track formation [46, 135] and sputtering [113] are described with the same value of λ, (2) SiO_2 in its amorphous phase illustrating the increase of the sensitivity of an amorphous material to high electronic excitation [136] and explaining the radial morphology of the track [62] and (3) track formation in $Y_3Fe_5O_{12}$ crystals to illustrate the velocity effect [18].

Taking crystalline SiO_2 quartz as typical case, λ = 3.8 nm is determined by fitting the track size (Fig. 2.18) with the i-TS model [113], assuming E_m, the energy necessary to melt the material, as the criterion to create a track. The sputtering rate Y_{tot} can be calculated within the framework of statistical thermodynamics (for details see [137]):

$$Y_{tot} = \int_0^\infty dt \int dr\, \Phi(T_a(r,t)) \text{ with } \Phi(T_a(r,t)) = N\sqrt{\frac{k_B\, T_a(r,t)}{2\pi\, m_{sp}}} \quad \exp\left(\frac{-U_s}{k_B T_a(r,t)}\right) \tag{2.20}$$

where m_{sp} is the mass of the sputtered atom and k_B the Boltzmann constant, $T_a(r,t)$ is the atomic temperature at a time t and at a distance r from the ion axis and U_s the known sublimation energy of crystalline SiO_2 [114]. In Fig. 2.18 measured and calculated track radii (filled dots and dashed line) and sputtering yields (open dots and solid line) for SiO_2 irradiated with an ion energy of 1 MeV/u are plotted versus the electronic energy loss. It is obvious that with the same value of the electron-phonon mean free path, λ = 3.6 nm, both track formation and sputtering yield can be described.

As described above for SiO_2 the electron-phonon mean free path was determined by fitting the track size in different amorphizable oxide materials [116]. It is clearly

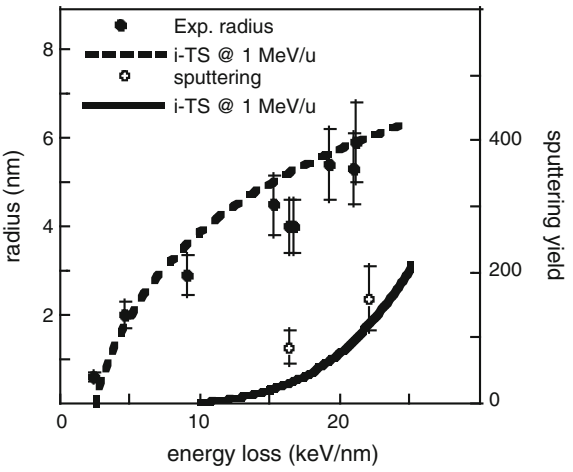

Fig. 2.18 Track radii [46] and sputtering rate [113] versus electronic energy loss for crystalline SiO_2 quartz. The lines correspond to the calculations with the i-TS model [113, 137]

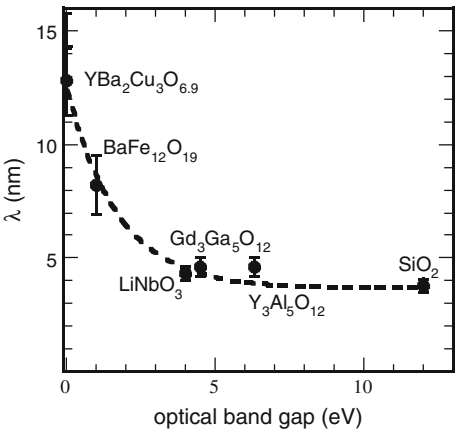

Fig. 2.19 Electron-phonon mean free path, λ, versus optical band gap energy for several amorphizable crystalline oxides [116] (figure partly extracted from [44])

to be seen in Fig. 2.19 that λ decreases monotonously with the band gap energy (E_G) of the materials investigated: the lower λ the larger the electron-phonon coupling. The decrease of λ is in agreement with the increase of the electron phonon coupling which increases with band gap energy [56]. According to Monte Carlo calculations, hot electrons in the conduction band cool down by an excitation of electrons from the valence band to the conduction band. The larger the band gap, the larger the cooling of the electrons and consequently the smaller the radial expansion of the energy to the electrons before its transfer to the atoms will be. If this correlation between the electron-phonon mean free path and the band gap energy (Fig. 2.19) is right [44] then there is no more free parameter in the i-TS model applied to crystalline insulators if E_m is known.

If E_m is not known, for materials with known gap energy at first the electron-phonon mean free path λ can be determined from its gap energy dependence as it is shown in Fig. 2.19 for the example of amorphizable oxides. Then with these values the energy necessary to melt the material, E_m, can be calculated by fitting the track radii versus the electronic energy deposition. In case of yttrium iron garnet ($Y_3Fe_5O_{12}$) with a gap energy of E_g = 2.8 eV an electron-phonon mean free path of λ = 5 nm is obtained from Fig. 2.19. For the calculation of E_m the fit of the track radii was limited to irradiations with beam energies less than 0.4 MeV/u yielding E_m = (0.55 ± 0.04) eV/at (see Fig. 2.20a) [47]. As expected this value is larger by 0.12 ± 0.04 eV/at than the energy necessary to reach the melting temperature which is equal to 0.43 eV/at. This value of 0.12 eV/at may correspond to the energy necessary to make the solid to liquid phase transition.

It is obvious in Fig. 2.20a that there is nearly no difference in the track radii in $Y_3Fe_5O_{12}$ for beam energies lower than 3.5 MeV/u while the radius is smaller for energies around 10 MeV/u. This is obviously a consequence of the different velocities in the two energy regions and the resulting different values of the mean absorption radius α. An explanation of this observation is possible by comparing the electron-phonon mean free path λ with the energy dependence of the mean

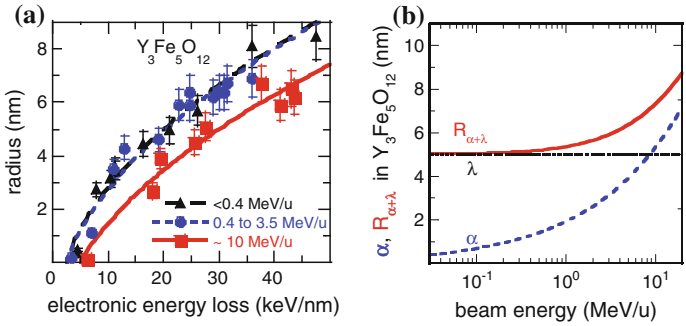

Fig. 2.20 **a** Calculation of the track radii in $Y_3Fe_5O_{12}$ measured at different beam energies (data points) for λ = 5 nm and an energy to reach the molten phase of E_m = 0.55 eV/at which takes into account the energy for the solid to liquid phase transition, (figure compiles data extracted from [47]). **b** Evolution of α (data from Fig. 2.3c) and $R_{\alpha+\lambda}$ versus beam energy for $Y_2Fe_5O_{12}$

absorption radius α for $Y_3Fe_5O_{12}$ (see Fig. 2.3c in Sect. 2.2.2). According to Fig. 2.3c the absorption radius α is equal to the electron-phonon mean free path λ at a beam energy of 10 MeV/u, $\alpha = \lambda = 5$ nm. Contrary, at smaller energies, here in the energy region between 0.04 and 3.5 MeV/u, λ is larger than α as illustrated in Fig. 2.20b. Consequently this λ value exceeds the radius in which the energy of the ions is initially deposited in the electronic system, i.e. the energy transfer to the atoms occurs in a larger radius compared to that of the initial energy deposition in the electronic system. But for energies in the order of 10 MeV/u and above the cylinder radius in which the energy is transferred to the atoms is determined by both λ and α. This radius $R_{\alpha+\lambda}$ is a convolution of both quantities and can be described by the relation $R^2_{\alpha+\lambda} = \alpha^2 + \lambda^2$. The dependence of $R_{\alpha+\lambda}$ on the ion energy is illustrated in Fig. 2.20b for $Y_3Fe_5O_{12}$ in comparison with the values of λ and α (from Fig. 2.3c) for this material. In the region of low energies, i.e. for energies <5 MeV/u, where α is smaller than λ, the deposition radius $R_{\alpha+\lambda}$ is nearly independent of the ion energy, i.e. the ion velocity does not remarkably modify the track radius in this region. In contrast, for energies >5 MeV/u, the volume in which the energy is deposited in the atomic system is mainly determined by α and remarkably influenced by the ion energy (Fig. 2.20b). Consequently, the initial energy is deposited in a larger volume leading to a smaller deposited energy density and, for a given threshold value of the electronic energy loss, S_{et}, to smaller track radii.

(B) *Amorphous versus crystalline material and radial track morphology.*

As the metallic materials, amorphous insulators are also more sensitive to electronic excitation than the same material in its crystalline phase. This will be illustrated in the following for the example of amorphous SiO_2 (a-SiO_2). The track size in a-SiO_2 was fitted by Rotaru et al. [136] and a value of λ = 3 nm was obtained for the electron-phonon mean free path, which is smaller than that of 3.6 nm for crystalline

quartz. In addition this material has a particular radial track morphology as found by SAXS measurements [62]: an under dense core is surrounded by an over dense shell. The experimental radii are plotted in Fig. 2.21 versus the Au ion energy ranging from 20 to 200 MeV. Using the electron-phonon mean free path λ = 3 nm, the track radius produced by Au ions consisting of the core+shell criterion (ΔE_m = 0.38 eV/at from a temperature of irradiation = 300 K). Now if using the energy to reach the boiling phase of the material which is the sum of the melting energy plus the energy to increase the temperature from T_m to T_b, the boiling temperature, plus the energy to make the liquid-boiling phase transition, the radii of the track core can be described using the same value of λ (Fig. 2.21). The use of the melting and boiling criteria was successfully applied to analyse specific responses in LiF [138, 139] and CaF_2 [61] in order to describe damage tracks resulting from the molten phase and from the boiling phase with the same electron-phonon coupling.

(C) *New developments for semiconductors.*

In a recent revue, Klaumünzer [30] makes several propositions for a further development of the thermal spike models. These models are not only used in ion-track physics, but also to describe the behaviour of free electrons and holes (carrier pairs) generated by femtosecond lasers [140, 141] in the case of band gap materials. Though these various models deal with similar physical problems, they do not take much notice of each other. The consequence is that knowledge, which has been gained in one field, is not transferred to the others.

First the description of track formation in semiconductors should take advantage of the knowledge of the value of the electron-phonon mean free time τ = 0.1 and 0.12 ps for Si and GaAs, respectively [142], as it was obtained from fs laser experiments. With these values of τ and with the relation $\lambda^2 = D_e(T_e)\ \tau$ with D_e = 2 $cm^2\ s^{-1}$ at high electronic temperature, the electron-phonon mean free path is $\lambda \sim 5$ nm for the two semiconductors. With such λ values Si and GaAs should be

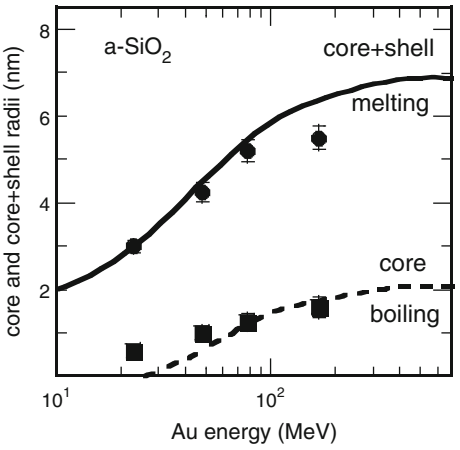

Fig. 2.21 Track radii in a-SiO_2 versus the Au ion energy. The points correspond to track radii in amorphous SiO_2 coresponding to a core (*squares*) and to core+shell (*dots*) structure as deduced from SAXS analysis [62]. The lines are the result of the calculations using the melting (*solid line*) and boiling (*dashed line*) criteria, respectively

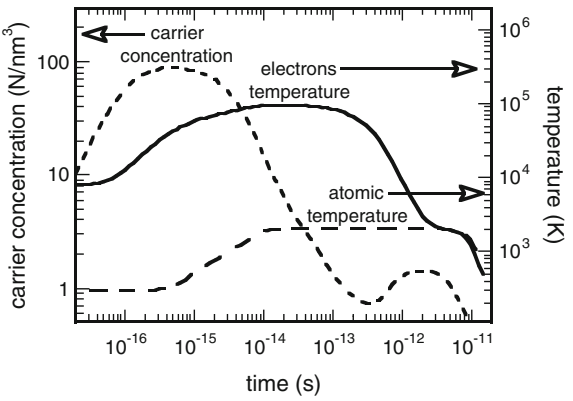

Fig. 2.22 The time evolution of the lattice temperature (*dashed line*), the electronic temperature (*solid line*) and the carrier concentration (*dotted line*) at the centre of an ion track in silicon resulting from an electronic energy deposition of 50 keV nm^{-1}(from [144])

sensitive to swift heavy ion irradiation in contrast to the results presented in Chap. 9. However, more experimental and theoretical studies are necessary in order to understand the differences between swift heavy ion and fs laser irradiation of semiconductors. For a discussion of this question the reader is referred to Sect. 2.3.2 and the paper of Sall et al. [143].

Second a severe deficiency in the currently used thermal spike models in ion track physics is the lack of taking into account the creation of electron-hole carriers. After a short time the carriers recombine, and the corresponding freed energy is transferred to the remaining electrons in the conduction band leading to an "electronic temperature". To take into account this physical phenomenon, Daraszewicz and Duffy [144] describe the creation of amorphous tracks in Si by taking into account the creation of electron-hole carriers. Instead of using the diffusion equation for the electrons [(2.6)] alone the authors try to model the fact that ionizing radiation in insulators results in a non equilibrium electron distribution, implying an excess of electrons in the conduction band connected with an increase of the number of holes in the valence band. This involves an energy confinement of the carriers. In the case of high electronic excitation carrier diffusion may be inhibited by the band gap gradient and the carriers may be confined. Such calculations have been done for Si by Daraszewicz and Duffy [144], and the time evolution of carrier concentration as well as lattice and electronic temperature are plotted versus time in Fig. 2.22. The energy given to the carriers is transferred to free electrons by carrier recombination and then transmitted to the lattice by electron-phonon coupling. If the lattice temperature exceeds the energy necessary to melt, amorphous tracks result from the quenching of the molten phase.

2.3.5.4 Combination of the Exciton with the Thermal Spike Model

The exciton decay model was recently developed for $LiNbO_3$ [145, 146] and for TiO_2 [38]. It is based on the synergy of nonradiative exciton decay and the

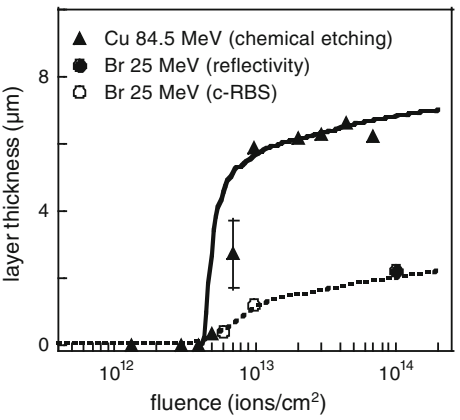

Fig. 2.23 Thickness of the amorphous layer in TiO_2 versus fluence for different irradiations [38]. The thickness of the amorphous layer was determined by chemical etching in case of the Cu irradiations, by means of reflectivity (*filled dots*) and channeling Rutherford backscattering (*open dots*) in case of Br irradiation at 25 MeV, respectively. The *solid lines* are obtained with the exciton model [38]

generated thermal spike. The non-radiative exciton decay leads to point defect-formation but it is only possible thanks to the energy provided by the thermal spike. The exciton model is described in detail in [146]. Another important point is that the model assumes that amorphization takes place when a critical defect concentration is reached, i.e., amorphization occurs as a defect driven transition whenever the stopping power of the ion exceeds the threshold value, S_{et}. Note that the model does not necessarily require melting as a process for amorphization.

The model was applied to $LiNbO_3$ and TiO_2. As example the depth evolution of the amorphous layer in TiO_2 was determined versus the ion fluence for different irradiations (see Fig. 2.23). The layer thickness values at an ion fluence of 10^{14} ions cm^{-2} for Cu and Br irradiations are 7 and 2 μm respectively. The different layer thicknesses that are amorphized are linked to the depth where the electronic energy loss threshold of track formation in TiO_2 by Cu and Br is reached. Using SRIM the corresponding electronic energy losses are then 4.7 and 5.3 keV/nm, respectively, leading to the electronic energy loss threshold of $\sim$5 keV nm^{-1} for amorphization of TiO_2.

2.4 Microscopic Models: Molecular Dynamics Approaches

Several molecular dynamics models have been developed to describe how the atoms behave after electronic excitation caused by the irradiation of matter with swift heavy ions. The following description will be separated in two parts: the first will be related to sputtering in the electronic regime and the second part will be devoted to track formation.

2.4.1 Sputtering by Electronic Excitation

The first molecular dynamics (MD) calculation was initiated by Urbassek et al. [64] to predict the emission yield of particles escaping from an argon crystal due to high electronic excitation. As a first approach it was assumed that sputtering is a consequence of a thermal spike. An idealized track is a cylinder in which the kinetic energy is deposited with a random direction of motion corresponding to thermal equilibrium. The atoms interact via a Lennard-Jones potential. The calculations show that there is a kind of two components in the angular distribution of the ejected particles: a jet perpendicular to the surface superimposed by a cosine distribution as observed in LiF [137]. As can be seen in Fig. 2.24 for the example of an Ar crystal, the sputtering yield (curve labelled as cylinder) follows a power law with $S_e^{3.3}$ for values of the electronic energy loss less than 0.6 keV nm^{-1} where the energy deposited in the atoms, E_0, is less than the sublimation energy, $U_{s,}$ while it is linear with S_e for $E_0 > U_s$. In a second approach proposed by Bringa [66], a Coulomb explosion was simulated in order to study the effect of this phenomenon on the sputter rate. It was found that the energy deposited in the atoms by a Coulomb explosion is thermalized in very short time so that the distribution of the emitted particles also consists of two components similar to the approach by Urbassek et al. [64]. Consequently, it will be difficult to distinguish between the effects of Coulomb explosion and thermal spike on the sputter process when only studying the shape of the angular distribution of the emitted particles.

The approaches described above were complemented recently by Beuve et al. [147] and Mookerjee et al. [65]. In this approach the energy transfer to the atoms is obtained by a numerical solution of (2.6) in Sect. 2.3.5 which describes the energy deposition in the electrons after the electron cascade, their energy diffusion and their energy transfer to the atoms via electron-phonon coupling defined by the electron-phonon mean free path λ [65]. The sputtering yields calculated for different values of λ are plotted versus the electronic energy loss in Fig. 2.24 and compared to the result of Urbassek et al. [64]. Clearly the threshold value for onset of sputtering is larger compared to the case of direct energy transfer to the atoms as

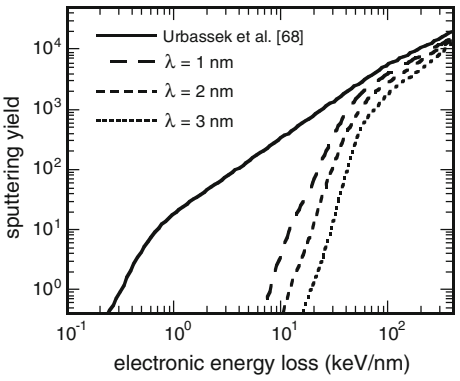

Fig. 2.24 Sputtering yield of an Ar crystal versus electronic energy loss. The *full line* is the result of MD calculations performed by Urbassek et al. [64]. The *dashed* and *dotted lines* are obtained in the framework of i-TS calculations using an electron-phonon mean free path of *1*, *2* and *3* nm (Mookerjee et al. [65])

assumed in the MD calculations (solid line in Fig. 2.24). The reason for this difference is that within the i-TS calculations the energy initially deposited in the electrons is reduced in the electronic subsystem by electron-electron interaction before it is transferred to the lattice atoms. Moreover, the threshold value increases with increasing value of the electron-phonon mean free path since the initial energy deposited in the electrons expands to the atoms in a larger volume. Near this threshold of sputtering for $S_e < 50$ keV nm^{-1}, the sputtering rate follows a power of ~ 5 with S_e independent of the λ value, reaching a power of one at larger S_e values like in the calculation of Urbassek et al. [64] for large S_e values.

In recent MD calculations by Huang et al. [148] it was tried to simulate the measured sputtering rate in UO_2 [149]. Using the approach developed by Beuve et al. [146] it was shown that the electron-phonon mean free path for UO_2, needed to reproduce the sputtering rate varies from 3 to 4 nm, depending on the value of the sublimation energy which was either obtained from the potential used for the MD calculation or from experiments, respectively. The value of 4 nm is not far from the value of 4.5 nm obtained from the systematic study of the electron-phonon mean free path as function of the band gap energy [44] in insulators (Fig. 2.19).

2.4.2 *Track Formation*

Several MD calculations to describe track formation have been performed following the approach by Urbassek et al. [64] where electronic excitations in the ion tracks are simulated as prompt cylindrical spikes whose energy is transferred to the atoms with a random direction of motion. Within this scheme a quantitative comparison with the experiment is difficult since in the electronic energy loss regime the energy deposition in the atoms is a complex combination of the initial energy deposition in the electrons as function of the incident ion velocity and the electron-phonon mean free path [109]. Moreover, in MD calculations the main problem consists in the development of realistic potentials that describe the main properties of the considered materials. However, the calculations follow the evolution of the energy transfer to the atoms as function of the time and give a final state of the material within the track at a time of around 10^{-10} s.

To show the strength of such MD predictions, Zhang et al. [2] analyzed the quenching states finally leading to the formation of an amorphous track in $Gd_2Ti_xZr_{2-x}O_7$, a class of pyrochlores for which it is well known that amorphization depends on the composition [150] (for details see Chap. 8). It is shown that the radial morphology of tracks in this material class can be reproduced by MD calculations, e.g. ranging from an amorphous track in $Gd_2Ti_2O_7$ to a complete defective fluorite structure in $Gd_2Zr_2O_7$. This is illustrated in Fig. 2.25 for the example of the intermediate composition with $x = 1$, i.e. for Gd_2TiZrO_7. In this case the track consists of an amorphous core surrounded by a defective fluorite shell. The difference between the real electronic energy loss of 2.2 GeV Au ions, $S_e =$ 40 keV nm^{-1} and the value used for the MD calculation, $S_e = 11$ keV nm^{-1}, is due

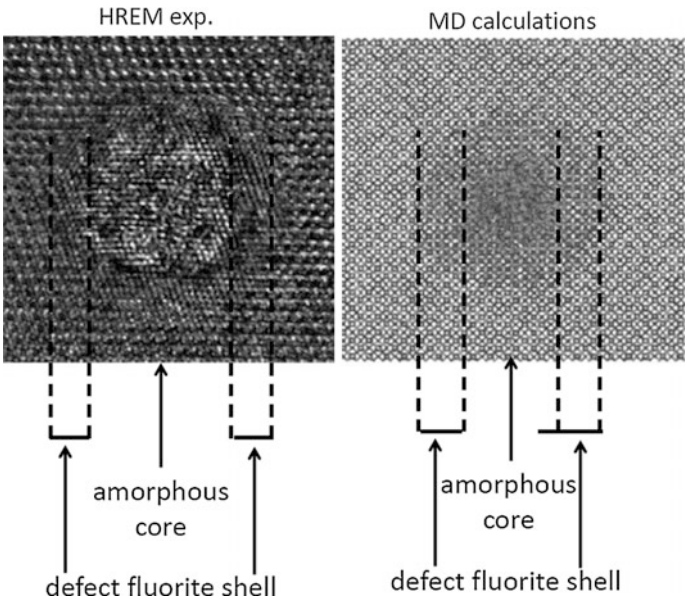

Fig. 2.25 HRTEM image of the morphology of an individual ion track produced by 2.2 GeV Au ions (S_e = 40 keV nm^{-1}) in Gd_2TiZrO_7 (*left*) that is reasonably reproduced by MD thermal spike calculations in Gd_2TiZrO_7, with an effective energy loss of 11 keV nm^{-1} (*right*) [2]

to the fact that the energy in case of the MD calculation is directly deposited in the atoms. MD calculations made by Pakarinen et al. [151] for crystalline SiO_2 and ZnO show different trends: tracks in SiO_2 become amorphous while in ZnO recrystallized tracks are observed.

In the case of graphite and diamond [66] for energy deposition within a cylinder of 3 nm radius, full amorphization of this region occurs during the first few picoseconds when the electronic energy loss is larger than (6.0 ± 0.9) keV nm^{-1} for graphite and (10.5 ± 1.5) keV nm^{-1} for diamond. These two values of electronic energy loss are "effective" since they correspond to an energy deposited in the 3 nm cylinder radius excluding any electronic energy diffusion prior to the transfer to the atoms. With another deposition model including energy diffusion to the electrons Pakarinen et al. [151] showed that the crystalline to amorphous transition in a diamond track should appear above a real electronic energy loss of 20 keV nm^{-1} if energy diffusion to the electrons is taken into consideration.

To illustrate the complexity of the description of track formation in insulators by MD calculations the core-shell structure of tracks observed in amorphous SiO_2 (a-SiO_2) [62] using small angle x-ray scattering (SAXS) [152] was calculated. The energy deposition profile was obtained from i-TS calculations [116] for Au ions with 1.1 MeV/u energy at the initial stage of the energy deposition. As previously described, such deposition profiles take into account the initial energy distribution of the electrons received from MC calculations. The energy then diffuses by

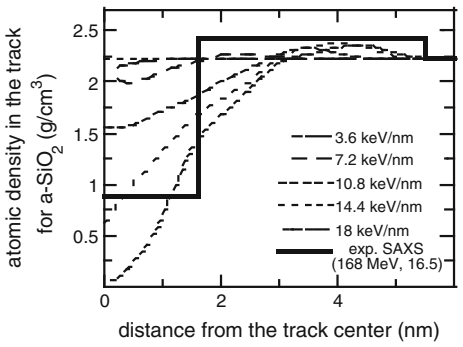

Fig. 2.26 Radial density profiles obtained from MD calculations for a-SiO_2 for different values of the electronic energy loss compared to the result of the SAXS experiment at 168 MeV irradiated a-SiO_2 [62]. The bulk density is 2.23 g/cm^3

electron-electron interactions before it is transferred to the atoms by electron-phonon coupling. The strength of this electron-phonon coupling is quantified by the electron-phonon mean free path (λ = 3 nm) which was obtained by fitting the track size in a-SiO_2 [136]. The electronic energy loss distribution was implemented in the code by an instantaneous deposition of kinetic energy in the atoms in a random direction. Now to model the anisotropic growth [129–131, 153] during track formation, MD calculations were performed for amorphous SiO_2 using the classical MD code [154–156]. The main principles of the molecular dynamics algorithms are described by Nordlund et al. [154] and Ghaly et al. [155]. The adaptive time step and electronic stopping algorithms are the same as in [154]. The atomic interactions were calculated using the Watanabe Si-O mixed system many-body potential [157, 158]. With such a model the observed permanent density changes in the track structure can be calculated by including the dynamics of the material transport. The simulations reveal a glass transition temperature of (2500 ± 500) K and a boiling temperature of (5500 ± 500) K for a-SiO_2 under superheating conditions, both in good agreement with the values used in the i-TS calculations. Figure 2.26 shows the radial density profiles achieved from the calculations for a-SiO_2 irradiated at various electronic energy depositions. All tracks consist of a low density core and a higher density shell in agreement with the SAXS measurements. The full line shows for comparison a density profile as deduced from SAXS measurements of samples irradiated with 168 MeV Au ions. The radii of the track cores obtained from the MD simulations for under-dense core and core +shell track radii, corresponding to the overall track size (under-dense core + over-dense shell), are plotted in Fig. 2.27 and agree with the SAXS measurements.

In conclusion, MD calculations are a good tool to describe the atomic rearrangement after this dense and nanometric energy deposition. However, a quantitative comparison with the experiment needs the knowledge of realistic values of the energy transfer to the atoms [62].

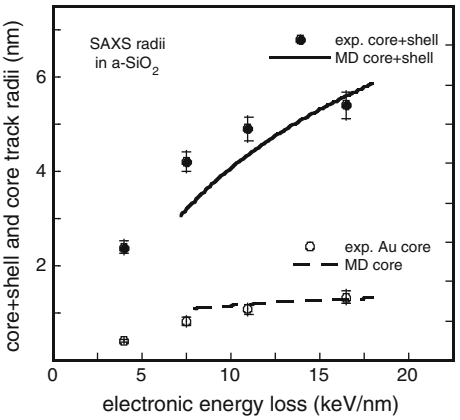

Fig. 2.27 Comparison of the calculated size of the track core (*dashed line*) and of the size of the core+shell track (*full line*) with SAXS radii for the core (*open dots*) and core +shell track (*filled dots*) measured by Kluth et al. [62]

2.4.3 Summary and Conclusions

The formation of tracks in materials irradiated in the electronic energy loss regime is the result of complex processes of energy deposition in the electrons, involving several steps on different time scales: (i) initial energy deposition in the electrons (10^{-17}–10^{-16} s), (ii) energy dissipation among the electrons (10^{-16}–10^{-14} s), leading to a radial expansion of the energy in a cylinder radius between 1 and 10 nm, and (iii) energy transfer to the atoms via the electron-phonon coupling (10^{-14}–10^{-12} s) leading to atomic motion and finally to the creation of a cylindrical damage along the ion path. The advantage to study the material transformation irradiated by swift heavy ions as compared to fs laser irradiation is given by a well-defined energy deposited in the electrons in a very short time and in a very small cylindrical volume. For most of fs laser irradiations, the electron energy excitation is created in a time of $\sim 10^{-14}$ s and the light is deposited in a volume of 0.5×0.5 μm^2 surface in a minimum depth of 10 nm. This planar geometry for the energy deposition leads to a cooling down time of the excited matter which is one order of magnitude larger than in the case of SHI.

In this chapter a review of the different models to describe the track formation are presented. There is an overall agreement on the time and on the radial distribution of energy deposition in the electrons using Monte Carlo calculations [19–25]. But several macroscopic models have been proposed to describe how this deposited energy is transferred to the atoms of the target: Coulomb explosion [32], reduced electronic energy loss [25], self-trapped exciton [36, 91], and bond weakening model [40]. The deficiency of these theoretical descriptions is the fact that they were tested on a very limited number of materials, one or two at most. Some more comparisons with numerous experimental results are needed to validate these descriptions. The only model applied to all kinds of materials, metallic materials, semiconductors and insulators, is the thermal spike model [42, 44, 48]. It was developed analytically [42] for insulators and semiconductors with two free parameters: there is a unique value of the initial radial energy deposition in the

atoms, whatever the beam energy is, using only a fraction of the energy deposited in the electrons that goes to the atoms. The numerical solution of the thermal spike model is most extensively studied [44, 48]: it takes into account (i) the initial energy deposition in the electrons obtained from Monte Carlo calculations normalized to the electronic energy loss, (ii) its evolution in the electronic system followed by (iii) its transfer to the atoms via electron-phonon coupling. The electron-phonon coupling is the only free parameter. The numerical development of the thermal spike model is powerful in describing (i) defect annealing [122], track defect creation [50], atomic mixing in metallic materials [159], (ii) track formation [116], sputtering [113] and the appearance of two thresholds of different damage creation [61, 62] in insulators, (iii) the deformation of Au nanoclusters embedded in a vitreous silica matrix [160]. However several critical examinations of the numerical solutions of the i-TS model were performed [30, 100] and the authors encourage the readers to go through these criticisms. One of the remaining questions is the description of irradiated semiconductors by this last model [63, 143] as mentioned in Chap. 9 of this book.

Aknowledgements Many thanks to S. Bouffard [25] and B. Canut [43] with whom I get deep discussions regarding their models. We would also like to thank E. Paumier who was with us when developing the numerical solutions of the inelastic thermal spike model. We would also deeply like to thank W. Wesch for critical and constructive reading of the manuscript.

References

1. M. Toulemonde, F. Studer, Phil. Mag. A **58**, 799 (1988)
2. J. Zhang, M. Lang, R.C. Ewing, R. Devanathan, W.J. Weber, M. Toulemonde, J. Mater. Res. **25**, 1345 (2010)
3. E. Balanzat, S. Bouffard, Sol. State Phenom. **30–31**, 7 (1993)
4. N. Bohr, Mat. Fys. Medd. **18**, 8 (1948)
5. J. Lindhard, M. Scharff, Phys. Rev. **124**, 128 (1961)
6. J. Lindhard, M. Scharff, H.E. Schiott, Mat Fys. Medd. **33**, 14 (1963)
7. J.P. Rozet, C. Stephan, D. Vernhet, Nucl. Instr. Meth. B **107**, 67 (1996)
8. P.L. Grande, G. Schiwietz, Nucl. Instr. Meth. B **267**, 859 (2009)
9. M. Toulemonde, Nucl. Instr. Meth. B **250**, 263 (2006)
10. J.P. Biersack, J.F. Ziegler, Nucl. Instr. Meth. **194**, 93 (1982)
11. J.F. Ziegler, Nucl. Instr. Meth. B **6**, 270 (1985)
12. P.L. Grande, G. Schiwietz, Adv. Quantum Chem. **45**, 7 (2004)
13. M. Toulemonde, F. Haas, Phys. Rev. C **15**, 49 (1977)
14. J.F. Ziegler, M.D. Ziegler, J.P. Biersack, Nucl. Instr. Meth. B **268**, 1818 (2010)
15. Y. Zhang, I.-T. Bae, K. Sun, C. Wang, M. Ishimaru, Z. Zhu, W. Jiang, W.J. Weber, J. Nucl. Mater. **389**, 303 (2009)
16. P. Sigmund, Mat. Fys. Medd. **52**, 557 (2006)
17. P. Sigmund, Eur. Phys. J. D **47**, 45 (2008)
18. A. Meftah, F. Brisard, J.M. Costantini, M. Hage-Ali, J.P. Stoquert, F. Studer, M. Toulemonde, Phys. Rev. B **48**, 920 (1993)
19. E.J. Kobetich, R. Katz, Phys. Rev. **170**, 391 (1968)
20. R. Katz, E.J. Kobetich, Phys. Rev. **186**, 344 (1969)

21. J. Fain, M. Monnin, M. Montret, Rad. Reas. **57**, 379 (1974)
22. C. Zhang, D.E. Dunn, R. Katz, Radiat. Protect. Dos. **13**, 215 (1985)
23. B. Gervais, S. Bouffard, Nucl. Instr. Meth. B **88**, 355 (1994)
24. G. Kraft, M. Krämer, Adv. Rad. Biol. **17**, 1 (1993)
25. S. Bouffard, C. Leroy, S. Della-Negra, A. Brunelle, J.M. Costantini, Phil. Mag. A **81**, 2841 (2001)
26. M.P.R. Waligorski, R.N. Hawn, R. Katz, Nucl. Track Rad. Meas. **11**, 309 (1986)
27. M. Toulemonde, W. Assmann, C. Dufour, A. Meftah, F. Studer, C. Trautmann, Mat. Fys. Medd. **52**, 263 (2006)
28. L.V. Zhigilei, D.S. Ivanov, E. Leveugle, SPIE **448**, 505 (2004)
29. M. Toulemonde, C. Dufour, E. Paumier, Phys. Rev. B **46**, 14362 (1992)
30. S. Klaumünzer, Mat. Fys. Medd. **52**, 293 (2006)
31. E. Silk, R. Barnes, Philos. Mag. **4**, 970 (1959)
32. R.L. Fleischer, P.B. Price, R.M. Walker, *Nuclear Tracks in Solids: Principles and Applications* (University of California, Berkeley, 1975)
33. D. Lesueur, A. Dunlop, Radiat. Eff. Defects Solids **126**, 163 (1993)
34. A. Iwase, N. Ishikawa, Y. Chimi, K. Tsuru, H. Wakana, O. Michikami, T. Kambara, Nucl. Instr. Meth. B **146**, 557 (1998)
35. K.S. Song, R.T. Williams, *Self Trapped Excitons* (Springer, Berlin, 1993)
36. N. Itoh, A.M. Stoneham, Nucl. Instr. Meth. B **146**, 362 (1998)
37. N. Itoh, D.M. Duffy, S. Khakshouri, A.M. Stoneham, J. Phys. Condens. Matter **21**, 474205 (2009)
38. A. Rivera, M.L. Crespillo, J. Olivares, R. Sanz, J. Jensen, F. Agulló-López, Nucl. Instr. Meth. B **268**, 3122 (2010)
39. J.A. van Vechten, R. Tsu, F.W. Saris, D. Hoonhout, Phys. Lett. A **74**(1979), 417 (1979)
40. P. Stampfli, K.H. Bennemann, Phys. Rev. B **49**(1994), 7299 (1994)
41. G. Szenes, Phys. Rev. B **51**, 8026 (1995)
42. G. Szenes, Phys. Rev. B **52**, 6154 (1995)
43. B. Canut, S.M.M. Ramos, Radiat. Eff. Defects Solids **145**, 1 (1998)
44. M. Toulemonde, Ch. Dufour, A. Meftah, E. Paumier, Nucl. Instr. Meth. B **166–167**, 903 (2000)
45. C. Trautmann, M. Toulemonde, C. Dufour, E. Paumier, Nucl. Instr. Meth. B **108**, 94 (1996)
46. A. Meftah, F. Brisard, J.M. Costantini, E. Dooryhée, M. Hage-Ali, M. Hervieu, J.P. Stoquert, F. Studer, M. Toulemonde, Phys. Rev. B **49**, 12457 (1994)
47. A. Meftah, M. Djebara, N. Khalfaoui, M. Toulemonde, Nucl. Instr. Meth. B **146**, 431 (1998)
48. Ch. Dufour, A. Audouard, F. Beuneu, J. Dural, J.P. Girard, A. Hairie, M. Levalois, E. Paumier, M. Toulemonde, J. Phys. Condens. Matter **5**, 4573, (1993)
49. Ch. Dufour, Z.G. Wang, E. Paumier, M. Toulemonde, Bull. Mater. Sci. **22**, 671 (1999)
50. Z.G. Wang, Ch. Dufour, E Paumier, M. Toulemonde, J. Phys. Condens. Matter **6**, 6733 (1994)
51. C. Dufour, B. Lesellier de Chezelles, V. Delignon, M. Toulemonde, E. Paumier, in *Proceedings of Conference on Chemical and Physical Modifications Induced by Irradiation in Glasses*, ed. by P. Mazzoldi (E-MRS, Strasbourg, 1992), p. 61
52. D.M. Duffy, S. Khakshouri, A.M. Rutherford, Nucl. Instr. Meth. **267**, 3050 (2009)
53. D.M. Duffy, S.L. Daraszewicz, J. Mulroue, Nucl. Instr. Meth. B **277**, 21 (2012)
54. C.P. Race, D.R. Mason, M.W. Finnis, W.M.C. Foulkes, A.P. Horsfield, A.P. Sutton, Rep. Prog. Phys. **73**, 116501 (2010)
55. M. Kaganov, I.M. Lifshitz, L.V. Tanatarov, Sov. Phys. JETP **4**, 173 (1957)
56. R.F. Haglund, R. Kelly, Mat. Fys. Medd. **43**, 527 (1992)
57. W. Hayes, A.M. Stoneham, in *Defects and Defect Processes in Nonmetallic Solids* (John Wiley and sons, New York, 1985)
58. H. Trinkaus, J. Nucl. Mater. **223**, 196 (1995)
59. A.L. Ryazanov, H. Trinkaus, A.E. Volkov, Phys. Rev. Lett. **84**, 919 (2000)
60. C. Trautmann, S. Klaumünzer, H. Trinkaus, Phys. Rev. Lett. **85**, 3648 (2000)

61. M. Toulemonde, A. Benyagoub, C. Trautmann, N. Khalfaoui, M. Boccanfuso, C. Dufour, F. Gourbilleau, J.J. Grob, J.P. Stoquert, J.M. Costantini, F. Haas, E. Jacquet, K.-O. Voss, A. Meftah, Phys. Rev. B **85**, 054112 (2012)
62. P. Kluth, C.S. Schnohr, O.H. Pakarinen, F. Djurabekova, D.J. Sprouster, R. Giulian, M.C. Ridgway, A.P. Byrne, C. Trautmann, D.J. Cookson, K. Nordlund, M. Toulemonde, Phys. Rev. Lett. **101**, 175503 (2008)
63. A. Kamarou, W. Wesch, E. Wendler, A. Undisz, M. Rettenmayr, Phys. Rev. **78**, 054111 (2008)
64. H.M. Urbassek, H. Kafemann, R.E. Johnson, Phys. Rev. B **49**, 786 (1994)
65. S. Mookerjee, M. Beuve, S.A. Khan, M. Toulemonde, A. Roy, Phys. Rev. B **78**, 045435 (2008)
66. E.M. Bringa, Nucl. Instr. Meth. B **209**, 1 (2003)
67. D. Schwen, E.M. Bringa, Nucl. Instr. Meth. B **256**, 187 (2007)
68. G. Schiwietz, K. Czerski, M. Roth, F. Staufenbiel, P.L. Grande, Nucl. Instr. Meth. B **226**, 6828 (2004)
69. G. Schiwietz, M. Beye, K. Czerski, A. Fohlisch, R. Konnecke, M. Roth, J. Schlappa, F. Staufenbiel, E. Suljoti, I. Kuusik, P.L. Grande, Nucl. Instr. Meth. B **317**, 48 (2013)
70. J. Rzadkiewicz, A. Gojska, O. Rosmej, M. Polasik, K. Słabkowska, Phys. Rev. A **82**, 012703 (2010)
71. A. Dunlop, D. Lesueur, Radiat. Eff. Defects Solids **126**, 123 (1993)
72. B. Canut, A. Benyagoub, G. Marest, A. Meftah, N. Moncoffre, S.M.M. Ramos, F. Studer, P. Thévenard, M. Toulemonde, Phys. Rev. B **51**, 12194 (1995)
73. N. Khalfaoui, J.P. Stoquert, F. Haas, C. Traumann, A. Meftah, M. Toulemonde, Nucl. Instr. Meth. B **286**, 247 (2012)
74. A. Dunlop, P. Legrand, D. Lesueur, N. Lorenzelli, J. Morillo, A. Barbu, S. Bouffard, Europhys. Lett. **15**, 765 (1991)
75. H. Dammak, D. Lesueur, A. Dunlop, P. Legrand, J. Morillo, Radiat. Eff. Defects Solids **126**, 111 (1993)
76. A. Dunlop, D. Lesueur, P. Legrand, H. Dammak, J. Dural, Nucl. Instr. Meth. B **90**, 330 (1994)
77. J.C. Phillips, Rev. Mod. Phys. **42**, 317 (1970)
78. M. Combescot, J. Bok, J. Benoit à la Guillaume, Phys. Rev. B **29**, 6393 (1984)
79. P. Baeri, J. de Phys. **44**, 157 (1983)
80. R.O. Bell, M. Toulemonde, P. Siffert, Appl. Phys. **19**, 313 (1979)
81. M. Toulemonde, R. Heddache, F. Nielsen, P. Siffert, J. Appl. Phys. **56**, 187 (1984)
82. M. Toulemonde, S. Unamuno, R. Heddache, M.O. Lampert, M. Hage-Ali, P. Siffert, Appl. Phys. A **36**, 31 (1985)
83. E. Fogarassy, R. Stuck, M. Toulemonde, D. Salles, P. Siffert, J. Appl. Phys. **54**, 5069 (1983)
84. F.A. Lindemann, Phys. Zeitschr. **11**, 609 (1910)
85. K. Sokolowski-Tinten, D. von der Linde, J. Phys. Condens. Matter **16**, 1517 (2004)
86. G. Sciaini, M. Harb, S.G. Kruglik, Th Payer, C.T. Hebeisen, F.J. Meyer zu Heringdorf, M. Yamaguchi, M. Horn von Hoegen, R. Ernstorfer, R.J.D. Miller, Nature **458**, 56 (2009)
87. L.D. Landau, Phys. Z. USSR **10**(1936), 154 (1936)
88. A.C. Lushchik, C.B. Lushchik, *Decay of Electronic Excitations with Defect Formation in Solids* (Nauka, Moscow, 1989)
89. N. Itoh, Adv. Phys. **31**, 49 (1982)
90. N. Itoh, D. Stoneham, Radiat. Eff. Defects Solids **155**, 277 (2001)
91. N. Itoh, Nucl. Instr. Meth. B **116**, 33 (1996)
92. A. Perez, E. Balanzat, J. Dural, Phys. Rev. B **41**, 3943 (1990)
93. K. Schwartz, C. Trautmann, A.S. El-Said, R. Neumann, M. Toulemonde, W. Knolle, Phys. Rev. B **70**, 184104 (2004)
94. R.C. Alig, S. Bloom, Phys. Rev. Lett. **35**, 1522 (1975)
95. F. Desauer, Z. Phys. **38**, 12 (1923)
96. L.T. Chadderton, H.M. Montagu-Pollock, Proc. Roy. Soc. London **A274**, 239 (1963)

97. F. Seitz, J.S. Koehler, Solid State Phys. **2**, 305 (1956)
98. P. Sigmund, C. Claussen, J. Appl. Phys. **52**, 990 (1981)
99. I.M. Lifshitz, M.I. Kaganov, L.V. Tanararov, J. Nucl. Energy A **12**, 69 (1960)
100. G. Szenes, Nucl. Instr. Meth. B **269**, 174 (2011)
101. B. Rethfeld, K. Sokolowski-Tinten, D. von der Linde, S.I. Anisimov, Phys. Rev. B **65**, 092103 (2002)
102. G. Szenes, K. Havancsak, V. Skuratov, P. Hanak, L. Zsoldos, T. Ungar, Nucl. Instr. Meth. B **166**, 933 (2000)
103. G. Szenes, Phys. Rev. B **70**, 094106 (2004)
104. G. Szenes, Radiat. Eff. Defects Solids **161**, 401 (2006)
105. J.M. Costantini, F. Brisard, J.L. Flament, A. Meftah, M. Toulemonde, M. Hage-Ali, Nucl. Instr. Meth. B **65**, 568 (1992)
106. J. Jensen, A. Dunlop, S. Della-Negra, M. Toulemonde, Nucl. Instr. Meth. B **146**, 412S (1998)
107. Ch. Houpert, F. Studer, D. Groult, M. Toulemonde, Nucl. Instr. Meth. B **39**, 720 (1989)
108. S. Moll, G. Sattonnay, L. Thomé, J. Jagielski, C. Legros, I. Monnet, Nucl. Instr. Meth. **268**, 2933 (2010)
109. M. Toulemonde, W. Assmann, C. Dufour, A. Meftah, C. Trautmann, Nucl. Instr. Meth. B **277**, 28 (2012)
110. N. Bonardi, PhD Thesis Université Claude Bernard, Lyon I, France, 1998
111. P. Hermes, B. Danielzik, N. Fabricius, D. von der Linde, J. Luhl, Y. Heppner, B. Stritzker, A. Pospieszczyk, Appl. Phys. A **39**, 9 (1986)
112. S.N. Luo, T.J. Ahrens, T. Cagin, W.A. III Goddard, D.C. Swift, A. Strachan, Phys Rev B **68**, 134206 (2003)
113. M. Toulemonde, W. Assmann, C. Trautmann, F. Grüner, Phys. Rev. Lett. **88**, 057602 (2002)
114. M. Toulemonde, W. Assmann, C. Trautmann, F. Grüner, H.D. Mieskes, H. Kucal, Z.G. Wang, Nucl. Instr. Meth. B **212**, 346 (2003)
115. M.D. Rodríguez, B. Afra, C. Trautmann, M. Toulemonde, T. Bierschenk, J. Leslie, R. Giulian, N. Kirby, P. Kluth, J. Non-Cryst. Solids **358**, 571 (2012)
116. A. Meftah, J.M. Costantini, N. Khalfaoui, S. Boudjadar, J.P. Stoquert, F. Studer, M. Toulemonde, Nucl. Instr. Meth. B **237**, 563 (2005)
117. M. Lang, M. Toulemonde, J. Zhang, F. Zhang, C.L. Tracy, J. Liang, Z. Wang, W.J. Weber, D. Severin, M. Bender, C. Trautmann, R.C. Ewing, Nucl. Instr. Meth. B **336**, 102 (2014)
118. Ch. Dufour, E. Paumier, M. Toulemonde, Nucl. Instr. Meth. B **122**, 445 (1997)
119. S.D. Brorson, A. Kazeroonian, J.S. Moodera, D.W. Face, T.K. Cheng, E.P. Ippen, M.S. Dresselhaus, G. Dresselhaus, Phys. Rev. Lett. **64**, 2172 (1990)
120. P.B. Allen, Phys. Rev. Lett. **59**, 1460 (1987)
121. G.H. Vineyard, Radiat. Eff. **29**, 245 (1976)
122. Z.G. Wang, C. Dufour, E. Paumier, M. Toulemonde, Nucl. Instr. Meth. B **115**, 577 (1996)
123. Ch. Dufour, F. Beuneu, E. Paumier, M. Toulemonde, Europhys. Lett. **45**, 585 (1999)
124. A. Audouard, E. Balanzat, J.C. Jousset, D. Lesueur, L. Thomé, J. Phys. Condens. Matter **5**, 995 (1993)
125. A. Audouard, J. Dural, M. Toulemonde, A. Lovas, G. Szenes, L. Thomé, Phys. Rev. B **54**, 15690 (1996)
126. A. Audouard, J. Dural, M. Toulemonde, A. Lovas, G. Szenes, L. Thomé, Nucl. Instr. Meth. B **107**, 185 (1996)
127. D.S. Sanditov, S.Sh. Sangadiev, B.D. Sanditov, Glass Phys. Chem. **26**, 59 (2000)
128. M.-D. Hou, S. Klaumünzer, G. Schumacher, Phys. Rev. B **41**, 1144 (1990)
129. A. Benyagoub, S. Loffler, R. Rammensee, S. Klaumunzer, Radiat. Eff. Defects Solids **110**, 217 (1989)
130. A. Benyagoub, S. Loffler, R. Rammensee, S. Klaumunzer, G. Saemann-Ischenko, Nucl. Instr. Meth. **65**, 228 (1992)
131. A. Benyagoub, S. Klaumunzer, M. Toulemonde, Nucl. Instr. Meth. B **146**, 449 (1998)

132. I.A. Baranov, YuV Martinenko, S.O. Tsepelevitch, YuN Yavlinskii, Sov. Phys. Usp. **31**, 1015 (1988)
133. O. Osmani, N. Medvedev, J.I. Juaristi, M. Schleberger, B. Rethfeld, Nucl. Instr. Meth. B **317**, 72 (2014)
134. B. Rethfeld, A. Rämer, N. Brouwer, N. Medvedev, O. Osmani, Nucl. Instr. Meth. B **327**, 78 (2014)
135. B. Afra, M.D. Rodriguez, C. Trautmann, O.H. Pakarinen, F. Djurabekova, K. Nordlund, T. Bierschenk, R. Giulian, M.C. Ridgway, G. Rizza, N. Kirby, M. Toulemonde, P. Kluth, J. Phys. Condens. Matter **25**, 045006 (2013)
136. C. Rotaru, F. Pawlak, N. Khalfaoui, C. Dufour, J. Perrière, A. Laurent, J.P. Stoquert, H. Lebius, M. Toulemonde, Nucl. Instr. Meth. B **272**, 9 (2012)
137. W. Assmann, M. Toulemonde, C. Trautmann, Top. Appl. Phys. **110**, 401 (2007)
138. C. Trautmann, M. Toulemonde, J.M. Costantini, J.J. Grob, K. Schwartz, Phys. Rev. B **62**, 13 (2000)
139. C. Trautmann, M. Toulemonde, K. Schwartz, J.M. Costantini, A. Müller, Nucl. Instr. Meth. B **164**(165), 365 (2000)
140. N.M. Bulgakova, R. Stoian, A. Rosenfeld, I.V. Hertel, E.E.B. Campbell, Phys. Rev. B **69**, 054102 (2004)
141. I.B. Bogatyrev, D. Grojo, P. Delaporte, S. Leyder, M. Sentis, W. Marine, T.E. Itina, J. Appl. Phys. **110**, 103106 (2011)
142. H.M. van Driel, Phys. Rev. B **35**, 8166 (1987)
143. M. Sall, I. Monnet, F. Moisy, C. Grygiel, S. Jublot-Leclerc, S. Della-Negra, M. Toulemonde, E. Balanzat, J. Mater. Sci. **50**, 5214 (2015)
144. S.L. Daraszewicz, D.M. Duffy, Nucl. Instr. Meth. B **269**, 1646 (2011)
145. F. Agullo-Lopez, A. Mendez, G. Garcia, J. Olivares, J.M. Cabrera, Phys. Rev. B **74**, 174106 (2006)
146. A. Rivera, A. Mendez, G. Garcia, J. Olivares, J.M. Cabrera, F. Agullo-Lopez, J. Lumin. **128**, 123 (2007)
147. M. Beuve, N. Stolterfoht, M. Toulemonde, C. Trautmann, H. Urbassek, Phys. Rev. B **68**, 125423 (2003)
148. M. Huang, D. Schwen, R.S. Averback, J. Nucl. Mat. **399**, 175 (2010)
149. S. Schlutig, Ph.D. Thesis, University of Caen, France, 2001, http://tel.archives-ouvertes.fr/tel-00002110/fr/
150. K.E. Sickafus, Science **289**, 748 (2000)
151. O.H. Pakarinen, F. Djurabekova, K. Nordlund, Nucl. Instr. Meth. B **268**, 3163 (2010)
152. A. Guinier, G. Fournet, *Small-Angle Scattering of X-rays* (John Wiley, New York, 1955)
153. A. Benyagoub, M. Toulemonde, J. Mater. Res. **30**, 1529 (2015)
154. K. Nordlund, M. Ghaly, R.S. Averback, M. Caturla, T.D. de la Rubia, J. Tarus, Phys. Rev. B **57**, 7556 (1998)
155. M. Ghaly, K. Nordlund, R.S. Averback, Phil. Mag A **79**, 795 (1999)
156. K. Nordlund, Comput. Mater. Sci. **3**, 448 (1995)
157. T. Watanabe, D. Yamasaki, K Tatsumura and I Ohdomari Appl. Surf. Sci. **234**, 207 (2004)
158. J. Samela, K. Nordlund, V.N. Popok, E.E.B. Campbell, Phys. Rev. B **77**, 075309 (2008)
159. Z.G. Wang, C. Dufour, S. Euphrasie, M. Toulemonde, Nucl. Instr. Meth. B **209**, 194 (2003)
160. C. Dufour, V. Khomenkov, G. Rizza, M. Toulemonde, J. Phys. Appl. Phys. **45**, 065302 (2012)
161. C.H. Houpert, M. Hervieu, F. Studer, D. Groult, M. Toulemonde, Nucl. Instr. Meth. B **39**, 720 (1989)
162. G. Schiwietz, G. Xiao, P.L. Grande, E. Luderer, R. Pazirandeh, U. Stettner, Europhys. Lett. **47**, 384 (1999)
163. L.E. Seiberling, C.K. Meins, B.H. Cooper, J.E. Griffith, M.H. Mendenhall, T.A. Tombrello, Nucl. Instr. Meth. **198**, 403 (1982)
164. G. Schiwietz, P.L. Grande, Phys. Rev. A **84**, 052703 (2011)

http://www.springer.com/978-3-319-33559-9

Ion Beam Modification of Solids
Ion-Solid Interaction and Radiation Damage
Wesch, W.; Wendler, E. (Eds.)
2016, XXIII, 534 p. 282 illus., Hardcover
ISBN: 978-3-319-33559-9